DOI: 10.13009/EUCASS2023-549
Aerospace Europe Conference 2023 – 10TH EUCASS – 9TH CEAS

Modeling and Stability Analysis of Sloshing on Liquid-Propelled Reusable Launch Vehicles

José Alfredo Macés-Hernández[⋆†], *David Seelbinder*[⋆] *and Stephan Theil*[⋆]
[⋆]*Guidance, Navigation and Control systems, Institute of Space Systems, German Aerospace Center (DLR)*
Robert-Hooke-Str. 7, 28359 Bremen, Germany
jose.maceshernandez / david.seelbinder / stephan.theil / @dlr.de
[†]Corresponding author

Abstract

The modeling of the liquid dynamics within the tanks of liquid-propelled vehicles is presented in this publication. The proposed model is valid for high-g environments, and planetary atmospheric flight, i.e., applicable to expendable Launch Vehicle (LV)s, Reusable Launch Vehicle (RLV)s and planetary landers. The oscillatory dynamics occurring at the top of the liquid's mass is approximated as the sum of n-swinging pendula representing the harmonic response of the n modes.

The interaction between the rigid body and pendula is tackled using a classic methodology from multibody systems, which is valid for a generic spacecraft with m tanks and n associated modes, i.e., the iterative Newton-Euler. The rationale behind the computation of the symbolic 3-Degrees of Freedom (DoF) model, and subsequent simplifications to a 2-DoF planar model, is thoroughly discussed. The former model is suitable for simulation, while the latter finds its applications for control design and stability analysis.

The symbolic computations were used to validate the *Symbolic Multibody Dynamics* toolbox belonging to the Guidance, Navigation and Control (GNC) systems department of the German Aerospace Center (DLR). This library can perform analytical computations of Equations of Motion (EoM)s for different configurations of multibody space systems, and at the same time, it is able to provide models that can be easily implemented in simulation environments.

The parameters associated to the liquids within the tanks of a space mission are calculated. They were derived using a set of analytical formulas corresponding to the geometry of the propellant and oxidizer tanks of a RLV. The stability analysis of the pair of complex poles and zeros associated to each mode is also studied, furthermore the position of the sloshing masses with regards to the danger zone is computed and analyzed. Finally, a Closed Loop (CL) analysis of the modes for a controller synthesized using $\mathcal{H}_\infty$ designed is presented in terms of the stability margins.

1. Introduction

Sloshing control has been an issue since the size liquid-propelled vehicles has grown as consequence of requiring heavier payloads deployed into orbit. For RLVs or planetary landers, a considerable amount of propellant is used to safely land the vehicle during the retro-propulsive burn. A large portion of the total vehicle's mass is hence composed of the liquids distributed within the fuel and oxidizer tanks.

The study of liquid motion within a cylindrical tank dates back to Poison and Rayleigh, who pioneered the computation of the first solutions to the harmonic oscillator problem, being the latter the introducer of Bessel functions to the solution.[3] During the sixties, the scientists developing the Saturn series of rockets, defined some of the models that are still being used to the date. Often they rely on a simplified form of the chaotic behavior happening on the liquid surface, yet they capture the core dynamics needed for the understanding of potential instabilities. The two main mechanical models are the spring-mass and the swinging pendulum, they were initially applied to a launch vehicle by Bauer,[3] largely benefiting from the advances in missile technology.[4,11,19]

Currently, more advanced and exact methods are available, they mostly rely on Computer Fluid Dynamics (CFD) methods for the characterization of the fluid dynamics, and while they allow a more accurate understanding of the liquid's behavior, they also rely on computations that are heavy and time expensive. Moreover, they cannot be easily deployed during control systems analysis and design across the all the stages of a space project, thus arising the need for models that are simple but also provide accurate results.

DOI: 10.13009/EUCASS2023-549

1.1 Parameters characterization

The most common arrangement for tank launch vehicles is one oxidizer and one fuel tanks per stage with solid boosters at each side;[32] this includes most of the operational launch vehicles available in the market today. Few alternatives, like the Delta IV in Heavy configuration[13] and the Falcon rocket in Heavy configuration, have liquid side boosters. On the other hand, conceptual[34] and flight-tested landers,[20] include a series of tanks distributed about the longitudinal axis in a ring configuration mostly due to dimension constraints.

For the purposes of this document, focus is on analyzing only the propellant and oxidizer tanks, which builds up most of the wet-mass of a vehicle during launch. The liquid needed for cold gas thrusters and/or the pressurization systems is usually much smaller, and consequently negligible.

There exist standard shapes used when designing spacecraft tanks, among the most common ones, there are cylindrical, cylindrical with elliptical domes, spherical, ellipsoidal or toroidal.[1] In some specific cases, the model of a cylindrical tank with flat domes is quite close to the one with spherical domes, mostly when the ratio between the dome length and the barrel length is small, thus making the same model valid for both cases. There are, however, studies with formulations to convert the parameter of the domed tank into a standard cylindrical shape,[15] this obviously result into a new virtual diameter and tank height. For the purposes of this article, we assume the ratio between the domes and barrel height to be small ($h_{\text{dome}}/h_{\text{barrel}} < 10\%$), hence the making available formulations found in the literature[1–3,25] valid for this study.

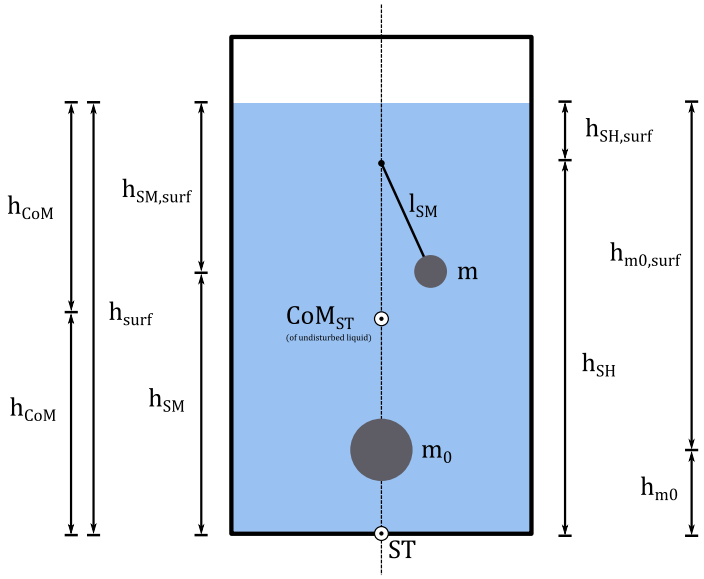

Figure 1: Cylindrical thank with one sloshing mode.

A cylindrical tank is depicted in Fig. 1, the parameters that characterize it are presented in Tab. 1. As a convention, the heights are measured positive in the direction bottom to top of the tank. These analytical formulations, are the combination of the contributions from several authors. Currently, modern references are the works from Ibrahim[12] and Dodge,[7] being the latter a re-edition of Abramson,[1] which is heavily based in the original work from Bauer.[3] The equations presented in Tab. 1 are a combination of all these sources, carefully verifying that the parameters here depicted actually correspond to those of the fluid model. Some unclear labeling has been found between editions, thus CFD has been used to validate each of the equations presented here. The reverse computation of the mechanical parameters from actual simulations -and eventual experiments- can be found in Yang.[33]

Some of the key considerations for this analysis are:

- The liquid is assumed to be an ideal fluid.
- The liquid is homogeneous and incompressible.
- The Bond number is assumed to be large enough (gravity dominated regime) such that the surface tension is negligible.

DOI: 10.13009/EUCASS2023-549

The total liquid mass for the j-th tank with n pendula(modes) is defined as[i]

$$m_{\text{liq}} = m_0 + \sum_{i=1}^{n} m_i \,. \tag{1}$$

The total Moment of Inertia (MoI) of the tanks arrangement wrt. the vehicle's Center of Mass (CoM) can be computed using the vector form of the Huygens-Steiner theorem[28]

$${}^{\square}\boldsymbol{J}_{\mathtt{o_B,liq}} = {}^{\square}\boldsymbol{J}_{\mathtt{m_0}} - m_0\left[\boldsymbol{S}({}^{\square}\boldsymbol{r}_{\mathtt{o_B,o_{SM_0}}})\right]^2 + \sum_{i=1}^{n} {}^{\square}\boldsymbol{J}_{\mathtt{m_1}} - m_i\left[\boldsymbol{S}({}^{\square}\boldsymbol{r}_{\mathtt{o_B,o_{SM_i}}})\right]^2 . \tag{2}$$

Remark 1 *For a single tank, the total MoI is a function of the static and the moving masses. Both components are a function of the true MoI and the relative position wrt. the analysis point (origin of the* B- *or* ST-*frame). The total MoI about the liquid's unperturbed CoM is assumed to be concentrated in the static component* ${}^{\square}\boldsymbol{J}_0$*, thus making the component associated to the i-th mode zero* $\left(\sum_{i=1}^{n} {}^{\square}\boldsymbol{J}_{\mathrm{SM}_i} = 0\right)$*. Hence, the contribution to the sloshing mass is only a function of the shift due to the change in position, mostly induced by lateral accelerations.*

For the computation of the specific parameters associated to each of the modes, the solutions to the Bessel function of the first kind are needed for the specific tank geometry. They can be found in the work from Bauer,[3] here repeated for the sake of simplicity $\left(\xi_1 = 1.8412\,,\ \xi_2 = 5.3314,\ \xi_3 = 8.5393,\ \xi_4 = 11.7060 \text{ and } \xi_i \approx \xi_{i\text{-}1} + \pi\right)$. Surprisingly, these solutions do not depend on the fluid properties, but rather on the geometry of the tank, thus making them generic for any liquid with a sufficiently large Bond number.

Table 1: Summary of the tank and sloshing mode parameters.

Parameter	**Equation**		**Units**
Total liquid mass	$m_{\text{liq}} = \frac{1}{4}\pi\rho_{\text{liq}}\mathsf{D}^2 h_{\text{liq}}$	(3)	(kg)
Total liquid CoM height [ii]	$h_{\text{CoM}} = \frac{1}{2}h_{\text{surf}}$	(4)	(m)
MoI of the solidified liquid	$J_0 = m_{\text{liq}}\left(\frac{1}{12}{h_{\text{liq}}}^2 + \frac{1}{16}\mathsf{D}^2\right)$	(5)	$(\text{kg}\cdot\text{m}^2)$
Total liquid MoI wrt. liquid CoM	$J_{\text{liq}} = J_0 + m_0\left(\frac{1}{2}h_{\text{liq}} + h_{\text{SM}_0}\right)^2 + \sum_{i=1}^{n} m_i\left(\frac{1}{2}h_{\text{liq}} + h_{\text{SM}_i}\right)^2$	(6)	$(\text{m}\cdot\text{kg}^2)$
i-th mode mass	$m_i = \frac{\mathsf{D}\tanh\left(\frac{2\xi_i h_{\text{liq}}}{\mathsf{D}}\right)m_{\text{liq}}}{\xi_i({\xi_i}^2 - 1)h_{\text{liq}}}$	(7)	(kg)
Surface height wrt. i-th hinge point[iii]	$h_{\mathtt{SH_i,surf}} = -\frac{\mathsf{D}}{\xi_i \sinh\left(\frac{2\xi_i h_{\text{surf}}}{\mathsf{D}}\right)}$	(8)	(m)
Hinge point height wrt. tank bottom	$h_{\text{SH}_i} = h_{\text{liq}} - h_{\mathtt{SH_i,surf}}$	(9)	(m)
Pendulum lever arm	$\ell_{\text{SM}i} = \frac{\mathsf{D}}{2\xi_i \tanh\left(\frac{\xi_i h_{\text{liq}}}{\mathsf{D}}\right)}$	(10)	(m)

[i] Index j was omitted from the equations to avoid abuse of notation.

[ii] The position of the fluid's CoM is found at half the distance of the total liquid height, and it was obtained by assuming that liquids behave as a solid under unperturbed conditions.

[iii] To respect the conservation of momentum, the computation of the static mass is done using the relative masses height wrt. the CoM of the solidified liquid. Here they are, however presented wrt. the bottom of the tank for easier understanding.

DOI: 10.13009/EUCASS2023-549

Surface height wrt. i-th mass	$h_{\mathtt{SM_i,surf}} = h_{\mathtt{SH_i,surf}} + \ell_{\mathtt{SM}i}$	(11)	(m)
Mass height wrt. tank bottom[iv]	$h_{\mathtt{SM}_i} = h_{\mathtt{liq}} - h_{\mathtt{SM_i,surf}}$	(12)	(m)
Mass length wrt. liquid CoM[iv]	$h_{\mathtt{CoM,SM_i}} = \dfrac{h_{\mathtt{liq}}}{2} - h_{\mathtt{SM_i,surf}}$	(13)	(m)
Sloshing mode natural frequency[v]	$\mathtt{f}_{\mathtt{SM}_i} = \dfrac{1}{2\pi}\sqrt{\dfrac{{}^{\mathtt{B}}\ddot{\mathtt{x}} - {}^{\mathtt{B}}g_{\mathtt{x}}}{\ell_{\mathtt{SM}i}}} = \dfrac{1}{2\pi}\sqrt{\dfrac{\Gamma}{\ell_{\mathtt{SM}i}}}$	(14)	(Hz)
Static mass	$m_0 = m_{\mathtt{liq}} - \sum_{i=1}^{n} m_i$	(15)	(kg)
Surface height wrt. static mass[vi]	$h_{\mathtt{SM_0,surf}} = h_{\mathtt{liq}} - h_{\mathtt{SM_0,surf}}$	(16)	(m)
Static mass height wrt. liquid CoM	$h_{\mathtt{CoM,SM_0}} = \sum_{i=1}^{n} \dfrac{m_i}{m_0} h_{\mathtt{CoM,SM_i}}$	(17)	(m)
Static mass height wrt. bottom of the tank	$h_{\mathtt{SM}_0} = \dfrac{h_{\mathtt{liq}}}{2} + h_{\mathtt{CoM,SM_0}}$	(18)	(m)

2. Dynamic modeling

2.1 Frames

For the description and analysis of the movement of the i-th pendulum with regards to the vehicle's CoM, some important frames, besides the classic body (B) and Earth-Fixed Up-East-North (EFUEN) frames, must be defined. For a flat and non-rotating Earth, the EFUEN-frame is considered as the inertial reference, thus expressed as I. The axes definition and rotation matrices are not presented here to keep this manuscript's length contained. They can, however, be found in our previous work[21] or derived from classic flight dynamics references.[5,6,30]

Remark 2 *The frames presented here below are defined for a single tank and a single mode/sloshing mass. For a real implementation, proper indexing must be chosen according to the real number of tanks and modes.*

1. **Tank frame (ST) :**

   - $o_{\mathtt{ST}}$: Found at the bottom of the j-tank.
   - $\hat{\boldsymbol{i}}_{\mathtt{ST}}$: Parallel to the j-tank's longitudinal axis. Positive in the direction from 0% to 100% filling level.
   - $\hat{\boldsymbol{j}}_{\mathtt{ST}}$: Pointing rightwards. Parallel to the tank's lateral axis.
   - $\hat{\boldsymbol{k}}_{\mathtt{ST}}$: Forms an orthonormal system. Parallel to the tank's normal axis.

   This frame is used for the representation of the equations presented in Sec. 1; all equations are referred to their origin. Those parameters are later used for the definition of the relative positions wrt. the vehicle's CoM. For this application, this frame is assumed aligned with the vehicle's structural (S) frame and so, body frame

$$ {}^{\mathtt{ST}}\boldsymbol{\mathcal{R}}_{\mathtt{S}} = {}^{\mathtt{ST}}\boldsymbol{\mathcal{R}}_{\mathtt{B}} = \mathbf{0}\,. \tag{19} $$

[iv] These assumptions hold true assuming the pendulum angle wrt. the tank longitudinal axis is zero.

[v] Element $\Gamma = \left(\left(\mathsf{T} - \mathcal{A}\right)/m_{\mathtt{tot}}\right)$ is the longitudinal component of the non-gravitational acceleration, also known as sensed acceleration. For a static tank, the frequency becomes only a function of the gravity.

[vi] Usually the position of the hinge is located below the hinge point for filling level above 50%, below this limit this value becomes negative and its limit tends towards zero as the filling level approaches zero.

DOI: 10.13009/EUCASS2023-549

2. **Pendulum-hinge frame (SH):**

   - o_{SH}: Located at the pendulum hinge point at the specific filling ratio.
   - $\hat{\boldsymbol{\imath}}_{\mathrm{SH}}$: Parallel to vector ${}^{\square}\boldsymbol{r}_{o_{\mathrm{B}},o_{\mathrm{SH}}}$, positive in direction o_{B} to o_{SH}.
   - $\hat{\boldsymbol{\jmath}}_{\mathrm{SH}}$: Pointing rightwards. This axis is parallel to the vehicle's lateral axis when θ_{SH} and ψ_{SH} are zero.
   - $\hat{\boldsymbol{k}}_{\mathrm{SH}}$: Completes an orthonormal system. It is parallel to the vehicle's directional axis when both angles are zero.

   The attitude of this frame coincides with the structural (S) and body frames (B) iff. the tank is placed along the vehicle's longitudinal axis. It changes its origin as the liquid mass is depleted. The rotation matrix is defined as

$$
{}^{\mathrm{SH}}\mathcal{R}_{\mathrm{S}} = {}^{\mathrm{SH}}\mathcal{R}_{\mathrm{B}} = \mathcal{R}_2(-\theta_{\mathrm{SH}})\,\mathcal{R}_3(\psi_{\mathrm{SH}}) = \begin{bmatrix} \cos\theta_{\mathrm{SH}} & 0 & \sin\theta_{\mathrm{SH}} \\ 0 & 1 & 0 \\ -\sin\theta_{\mathrm{SH}} & 0 & \cos\theta_{\mathrm{SH}} \end{bmatrix} \begin{bmatrix} \cos\psi_{\mathrm{SH}} & \sin\psi_{\mathrm{SH}} & 0 \\ -\sin\psi_{\mathrm{SH}} & \cos\psi_{\mathrm{SH}} & 0 \\ 0 & 0 & 1 \end{bmatrix}. \tag{20}
$$

3. **Pendulum-mass frame (SM):**

   - o_{SM}: Located at the CoM of the i-th sloshing mass.
   - $\hat{\boldsymbol{\imath}}_{\mathrm{SM}}$: Parallel to the vector ${}^{\square}\boldsymbol{r}_{o_{\mathrm{SM}},o_{\mathrm{SH}}}$, positive in direction from o_{SM} to o_{SH}.
   - $\hat{\boldsymbol{\jmath}}_{\mathrm{SM}}$: Contained in the vehicle pitch plane, coincident with the vehicle's lateral axis when the liquid is unperturbed.
   - $\hat{\boldsymbol{k}}_{\mathrm{SM}}$: Contained in the vehicle yaw plane, coincident with the vehicle's directional axis when the liquid is unperturbed.

   This frame rotates and changes position as the mass moves (the liquid inside the tank sloshes). It also changes its origin as the liquid is depleted. The rotation matrix is defined as

$$
{}^{\mathrm{SM}}\mathcal{R}_{\mathrm{S}} = {}^{\mathrm{SM}}\mathcal{R}_{\mathrm{B}} = \mathcal{R}_2(\theta_{\mathrm{SM}})\,\mathcal{R}_3(-\psi_{\mathrm{SM}}) = \begin{bmatrix} \cos\theta_{\mathrm{SM}} & 0 & -\sin\theta_{\mathrm{SM}} \\ 0 & 1 & 0 \\ \sin\theta_{\mathrm{SM}} & 0 & \cos\theta_{\mathrm{SM}} \end{bmatrix} \begin{bmatrix} \cos\psi_{\mathrm{SM}} & -\sin\psi_{\mathrm{SM}} & 0 \\ \sin\psi_{\mathrm{SM}} & \cos\psi_{\mathrm{SM}} & 0 \\ 0 & 0 & 1 \end{bmatrix}. \tag{21}
$$

   A graphic description of the axes and angles is depicted in Fig. 2 in three-dimensional (3D) coordinates and in Fig. 3 for planar configuration.

2.2 Pendulum dynamics

Remark 3 *The modeling presented here below is described for a single mode and a single tank, it can however, be extended for multiple modes and multiple tanks.*

As explained in Sec. 1.1, the static mass is assumed to be part of the vehicle's dry mass, as well as the MoI. The mass distribution for a vehicle with a single tank and n-modes is defined as follows:

$$
m_{\mathrm{tot}} = \underbrace{m_{\mathrm{B_{dry}}} + m_0}_{m_{\mathrm{B}}} + \sum_{i=1}^{n} m_i\,. \tag{22}
$$

Following Remark 1, the total MoI of the tank is only a contribution of the MoI about the CoM of the liquid mass; the associated n-modes are thus inertia-less, and their contribution is only a function of the mass itself and the lateral positions shift

$$
{}^{\mathrm{B}}\boldsymbol{J}_{\mathrm{tot}} = \underbrace{{}^{\mathrm{B}}\boldsymbol{J}_{\mathrm{B_{dry}}} + {}^{\mathrm{B}}\boldsymbol{J}_{o_{\mathrm{B}},\mathrm{m}_0}}_{{}^{\mathrm{B}}\boldsymbol{J}_{\mathrm{B}}} + \sum_{i=1}^{n} {}^{\mathrm{B}}\boldsymbol{J}_{o_{\mathrm{B}},\mathrm{m_i}} = {}^{\mathrm{B}}\boldsymbol{J}_{\mathrm{B}} + \sum_{i=1}^{n} \left(\cancelto{\boldsymbol{0}}{{}^{\mathrm{B}}\boldsymbol{J}_{\mathrm{m}_i}} - m_i \left[\boldsymbol{S}({}^{\mathrm{B}}\boldsymbol{r}_{o_{\mathrm{B}},o_{\mathrm{SM_i}}}) \right]^2 \right). \tag{23}
$$

The considered spherical pendulum has 2-DoF; its attitude is described by two angles; θ_{SM} about the $\hat{\boldsymbol{\jmath}}_{\mathrm{SM}}$-axis and ψ_{SM} about $\hat{\boldsymbol{k}}_{\mathrm{SM}}$-axis.

DOI: 10.13009/EUCASS2023-549

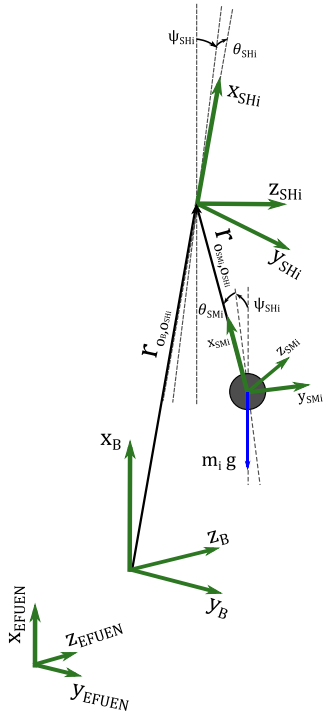

Figure 2: Principal sloshing frames in 3D.

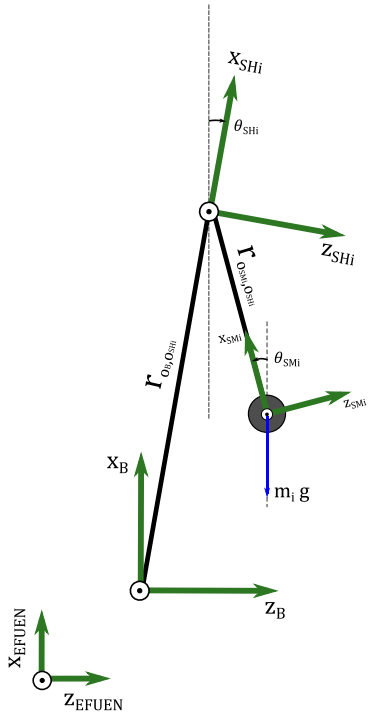

Figure 3: Principal sloshing frames in 2D.

The position of $o_{\mathtt{SH}}$ wrt. the i-th mass origin $o_{\mathtt{SM}}$ is represented by

$$^{\mathtt{SM}}\boldsymbol{r}_{o_{\mathtt{SM}},o_{\mathtt{SH}}} = \begin{bmatrix} \ell_{\mathtt{SM}} & 0 & 0 \end{bmatrix}^{\top}, \tag{24}$$

and the hinge point position wrt. the vehicle's CoM by

$$^{\mathtt{SH}}\boldsymbol{r}_{o_{\mathtt{B}},o_{\mathtt{SH}}} = \begin{bmatrix} \ell_{\mathtt{SH}} & 0 & 0 \end{bmatrix}^{\top}, \tag{25}$$

both position vectors have a single element in the first component when represented in frames SH and SM, respectively.

The position of $o_{\mathtt{SM}}$ wrt. $o_{\mathtt{B}}$ is denoted by

$$^{\square}\boldsymbol{r}_{o_{\mathtt{B}},o_{\mathtt{SM}}} = {}^{\square}\boldsymbol{r}_{o_{\mathtt{SH}},o_{\mathtt{SM}}} + {}^{\square}\boldsymbol{r}_{o_{\mathtt{B}},o_{\mathtt{SH}}}, \tag{26}$$

in any given frame $\square$.

For what regards the linear velocity

$$^{\mathtt{B}}_{\mathtt{I}}\dot{\boldsymbol{r}}_{o_{\mathtt{E}},o_{\mathtt{SM}}} = {}^{\mathtt{B}}_{\mathtt{I}}\dot{\boldsymbol{r}}_{o_{\mathtt{E}},o_{\mathtt{B}}} + {}^{\mathtt{B}}_{\mathtt{I}}\dot{\boldsymbol{r}}_{o_{\mathtt{B}},o_{\mathtt{SM}}}, \tag{27}$$

and linear acceleration

$$^{\mathtt{B}}_{\mathtt{I},\mathtt{I}}\ddot{\boldsymbol{r}}_{o_{\mathtt{E}},o_{\mathtt{SM}}} = {}^{\mathtt{B}}_{\mathtt{I},\mathtt{I}}\ddot{\boldsymbol{r}}_{o_{\mathtt{E}},o_{\mathtt{B}}} + {}^{\mathtt{B}}_{\mathtt{I},\mathtt{I}}\ddot{\boldsymbol{r}}_{o_{\mathtt{B}},o_{\mathtt{SM}}}, \tag{28}$$

computed from Eq. 26, it must be noted that the derivatives are performed in I-frame; however, the vector is expressed in B-frame, it is indeed also possible, to change the frame of reference via an adequate rotation matrix ($\boldsymbol{\mathcal{R}}$).

It is known that the vehicle's inertial acceleration in B-frame coordinates ($^{\mathtt{B}}_{\mathtt{I}}\ddot{\boldsymbol{r}}_{o_{\mathtt{E}},o_{\mathtt{B}}} = {}^{\mathtt{B}}\boldsymbol{\mathcal{R}}_{\mathtt{I}}\,{}^{\mathtt{I}}\boldsymbol{a}_{o_{\mathtt{E}},o_{\mathtt{B}}} = \begin{bmatrix} {}^{\mathtt{B}}\ddot{\mathtt{x}} & {}^{\mathtt{B}}\ddot{\mathtt{y}} & {}^{\mathtt{B}}\ddot{\mathtt{z}} \end{bmatrix}$) is given by the following relationship

$$^{\mathtt{B}}_{\mathtt{I},\mathtt{I}}\ddot{\boldsymbol{r}}_{o_{\mathtt{E}},o_{\mathtt{B}}} = {}^{\mathtt{B}}_{\mathtt{B},\mathtt{I}}\ddot{\boldsymbol{r}}_{o_{\mathtt{E}},o_{\mathtt{B}}} + {}^{\mathtt{B}}\boldsymbol{\omega}_{\mathtt{I},\mathtt{B}} \times {}^{\mathtt{B}}_{\mathtt{I}}\dot{\boldsymbol{r}}_{o_{\mathtt{E}},o_{\mathtt{B}}}, \tag{29}$$

where the inertial velocity in B-frame coordinates is defined by $^{\mathtt{B}}_{\mathtt{I}}\dot{\boldsymbol{r}}_{o_{\mathtt{E}},o_{\mathtt{B}}} = \begin{bmatrix} \mathtt{u} & \mathtt{v} & \mathtt{w} \end{bmatrix}^{\top}$ and its derivative in B-frame as $^{\mathtt{B}}_{\mathtt{B},\mathtt{I}}\ddot{\boldsymbol{r}}_{o_{\mathtt{E}},o_{\mathtt{B}}} = \begin{bmatrix} \dot{\mathtt{u}} & \dot{\mathtt{v}} & \dot{\mathtt{w}} \end{bmatrix}^{\top}$.

For the computation of velocities on the Right-Hand Side (RHS) of Eq. 22

$$^{\mathtt{B}}_{\mathtt{I}}\dot{\boldsymbol{r}}_{o_{\mathtt{B}},o_{\mathtt{SM}}} = {}^{\mathtt{B}}\boldsymbol{\mathcal{R}}_{\mathtt{SH}}\,{}^{\mathtt{SH}}_{\mathtt{I}}\dot{\boldsymbol{r}}_{o_{\mathtt{B}},o_{\mathtt{SH}}} + {}^{\mathtt{B}}\boldsymbol{\mathcal{R}}_{\mathtt{SM}}\,{}^{\mathtt{SM}}_{\mathtt{I}}\dot{\boldsymbol{r}}_{o_{\mathtt{SH}},o_{\mathtt{SM}}}, \tag{30}$$

DOI: 10.13009/EUCASS2023-549

and accelerations on the RHS of Eq. 29

$$ {}^{\mathtt{B}}_{\mathtt{I},\mathtt{I}}\ddot{\boldsymbol{r}}_{o_{\mathtt{B}},o_{\mathtt{SM}}} = {}^{\mathtt{B}}\boldsymbol{\mathcal{R}}_{\mathtt{SH}}\, {}^{\mathtt{SH}}_{\mathtt{I},\mathtt{I}}\ddot{\boldsymbol{r}}_{o_{\mathtt{B}},o_{\mathtt{SH}}} + {}^{\mathtt{B}}\boldsymbol{\mathcal{R}}_{\mathtt{SM}}\, {}^{\mathtt{SM}}_{\mathtt{I},\mathtt{I}}\ddot{\boldsymbol{r}}_{o_{\mathtt{SH}},o_{\mathtt{SM}}}, \tag{31} $$

they are defined as a function of the first and second derivatives of positions 25 and 24. This step is crucial given the fact that those position vectors have a single element, thus the resulting derivatives are also single element when performed in SH- and SM-frame, respectively.

Given the fact that the liquid level is assumed to be decreasing slowly, the rate of change in attitude SH-frame is close to zero. Consequently, the following angular velocities and angular accelerations of the SH-frame wrt. the inertial reference can be simplified to

$$ {}^{\mathtt{SH}}\square_{\mathtt{I},\mathtt{SH}} = {}^{\mathtt{SH}}\square_{\mathtt{I},\mathtt{B}} + \cancelto{\boldsymbol{0}}{{}^{\mathtt{SH}}\square_{\mathtt{B},\mathtt{SH}}} = {}^{\mathtt{SH}}\square_{\mathtt{I},\mathtt{B}}, \qquad \text{where } \square = \left(\boldsymbol{\omega}, \boldsymbol{\alpha}\right), \tag{32} $$

and in the same fashion, the angular velocity and angular acceleration of the mass wrt. the I-frame

$$ {}^{\mathtt{SM}}\square_{\mathtt{I},\mathtt{SM}} = {}^{\mathtt{SM}}\square_{\mathtt{I},\mathtt{SH}} + {}^{\mathtt{SM}}\square_{\mathtt{SH},\mathtt{SM}}, \qquad \text{where } \square = \left(\boldsymbol{\omega}, \boldsymbol{\alpha}\right), \tag{33} $$

recall the body angular velocity as ${}^{\mathtt{B}}\boldsymbol{\omega}_{\mathtt{I},\mathtt{B}} = \begin{bmatrix}\mathtt{p} & \mathtt{q} & \mathtt{r}\end{bmatrix}^{\top}$, and the body angular acceleration as ${}^{\mathtt{B}}\boldsymbol{\alpha}_{\mathtt{I},\mathtt{B}} = \begin{bmatrix}\alpha_1 & \alpha_2 & \alpha_3\end{bmatrix}^{\top}$.

The angular velocity

$$ {}^{\mathtt{SM}}\boldsymbol{\omega}_{\mathtt{B},\mathtt{SM}} = {}^{\mathtt{SM}}\boldsymbol{\mathcal{T}}_{\mathtt{I}}\, {}^{\mathtt{SM}}\dot{\boldsymbol{\varepsilon}}_{\mathtt{B}} = \begin{bmatrix}1 & 0 & -\sin\theta_{\mathtt{SM}} \\ 0 & 1 & 0 \\ 0 & 0 & \cos\theta_{\mathtt{SM}}\end{bmatrix}\begin{bmatrix}0 \\ \dot{\theta}_{\mathtt{SM}} \\ -\dot{\psi}_{\mathtt{SM}}\end{bmatrix} = \begin{bmatrix}\dot{\psi}_{\mathtt{SM}}\sin\theta_{\mathtt{SM}} \\ \dot{\theta}_{\mathtt{SM}} \\ -\dot{\psi}_{\mathtt{SM}}\cos\theta_{\mathtt{SM}}\end{bmatrix}, \tag{34} $$

and angular acceleration is thus rewritten

$$ {}^{\mathtt{SM}}\boldsymbol{\alpha}_{\mathtt{B},\mathtt{SM}} = {}^{\mathtt{SM}}\boldsymbol{\mathcal{T}}_{\mathtt{B}}\, {}^{\mathtt{SM}}\ddot{\boldsymbol{\varepsilon}}_{\mathtt{B}} + {}^{\mathtt{SM}}\dot{\boldsymbol{\mathcal{T}}}_{\mathtt{B}}\, {}^{\mathtt{SM}}\dot{\boldsymbol{\varepsilon}}_{\mathtt{B}} = \begin{bmatrix}1 & 0 & -\sin\theta_{\mathtt{SM}} \\ 0 & 1 & 0 \\ 0 & 0 & \cos\theta_{\mathtt{SM}}\end{bmatrix}\begin{bmatrix}0 \\ \ddot{\theta}_{\mathtt{SM}} \\ -\ddot{\psi}_{\mathtt{SM}}\end{bmatrix} + \begin{bmatrix}0 & 0 & -\dot{\theta}_{\mathtt{SM}}\cos\theta_{\mathtt{SM}} \\ 0 & 0 & 0 \\ 0 & 0 & -\dot{\theta}_{\mathtt{SM}}\sin\theta_{\mathtt{SM}}\end{bmatrix}\begin{bmatrix}0 \\ \dot{\theta}_{\mathtt{SM}} \\ -\dot{\psi}_{\mathtt{SM}}\end{bmatrix} = \begin{bmatrix}\ddot{\psi}_{\mathtt{SM}}\sin\theta_{\mathtt{SM}} + \dot{\theta}_{\mathtt{SM}}\dot{\psi}_{\mathtt{SM}}\cos\theta_{\mathtt{SM}} \\ \ddot{\theta}_{\mathtt{SM}} \\ \dot{\theta}_{\mathtt{SM}}\dot{\psi}_{\mathtt{SM}}\sin\theta_{\mathtt{SM}} - \ddot{\psi}_{\mathtt{SM}}\cos\theta_{\mathtt{SM}}\end{bmatrix}, \tag{35} $$

as a function of the first and second derivatives of the pendulum's Euler angles.

Recall ${}^{\mathtt{SM}}\boldsymbol{\varepsilon}_{\mathtt{B}} = \begin{bmatrix}0 & \theta_{\mathtt{SM}} & \psi_{\mathtt{SM}}\end{bmatrix}^{\top}$, ${}^{\mathtt{SM}}\boldsymbol{\omega}_{\mathtt{B},\mathtt{SH}} = \boldsymbol{0}$, thus ${}^{\mathtt{SH}}\boldsymbol{\omega}_{\mathtt{I},\mathtt{SH}} = {}^{\mathtt{SH}}\boldsymbol{\mathcal{R}}_{\mathtt{B}}\begin{bmatrix}\mathtt{p} & \mathtt{q} & \mathtt{r}\end{bmatrix}^{\top}$; and ${}^{\mathtt{SH}}\boldsymbol{\alpha}_{\mathtt{B},\mathtt{SH}} = \boldsymbol{0}$, thus ${}^{\mathtt{SH}}\boldsymbol{\alpha}_{\mathtt{I},\mathtt{SH}} = {}^{\mathtt{SH}}\boldsymbol{\mathcal{R}}_{\mathtt{B}}\begin{bmatrix}\alpha_1 & \alpha_2 & \alpha_3\end{bmatrix}^{\top}$.

Under earlier assumptions, the expanded velocities on the RHS of Eq. 30 are

$$ {}^{\mathtt{SH}}_{\mathtt{I}}\dot{\boldsymbol{r}}_{o_{\mathtt{B}},o_{\mathtt{SH}}} = \cancelto{\boldsymbol{0}}{{}^{\mathtt{SH}}_{\mathtt{SH}}\dot{\boldsymbol{r}}_{o_{\mathtt{B}},o_{\mathtt{SH}}}} + \underbrace{{}^{\mathtt{SH}}\boldsymbol{\omega}_{\mathtt{I},\mathtt{SH}}}_{{}^{\mathtt{SH}}\boldsymbol{\omega}_{\mathtt{I},\mathtt{B}}} \times {}^{\mathtt{SH}}\boldsymbol{r}_{o_{\mathtt{B}},o_{\mathtt{SH}}}, \tag{36} $$

and

$$ {}^{\mathtt{SM}}_{\mathtt{I}}\dot{\boldsymbol{r}}_{o_{\mathtt{SH}},o_{\mathtt{SM}}} = \cancelto{\boldsymbol{0}}{{}^{\mathtt{SM}}_{\mathtt{SH}}\dot{\boldsymbol{r}}_{o_{\mathtt{SH}},o_{\mathtt{SM}}}} + {}^{\mathtt{SM}}\boldsymbol{\omega}_{\mathtt{I},\mathtt{SM}} \times {}^{\mathtt{SM}}\boldsymbol{r}_{o_{\mathtt{SH}},o_{\mathtt{SM}}}, \tag{37} $$

while accelerations on the RHS of Eq. 31 are

$$ {}^{\mathtt{SH}}_{\mathtt{I},\mathtt{I}}\ddot{\boldsymbol{r}}_{o_{\mathtt{B}},o_{\mathtt{SH}}} = \cancelto{\boldsymbol{0}}{{}^{\mathtt{SH}}_{\mathtt{SH},\mathtt{SH}}\ddot{\boldsymbol{r}}_{o_{\mathtt{B}},o_{\mathtt{SH}}}} + \underbrace{{}^{\mathtt{SH}}\boldsymbol{\alpha}_{o_{\mathtt{B}},o_{\mathtt{SH}}}}_{{}^{\mathtt{SH}}\boldsymbol{\alpha}_{\mathtt{I},\mathtt{B}}} \times {}^{\mathtt{SH}}\boldsymbol{r}_{o_{\mathtt{B}},o_{\mathtt{SH}}} + 2\underbrace{{}^{\mathtt{SH}}\boldsymbol{\omega}_{\mathtt{I},\mathtt{SH}}}_{{}^{\mathtt{SH}}\boldsymbol{\omega}_{\mathtt{I},\mathtt{B}}} \times \cancelto{\boldsymbol{0}}{{}^{\mathtt{SH}}_{\mathtt{SH}}\dot{\boldsymbol{r}}_{o_{\mathtt{B}},o_{\mathtt{SH}}}} + \underbrace{{}^{\mathtt{SH}}\boldsymbol{\omega}_{\mathtt{I},\mathtt{SH}}}_{{}^{\mathtt{SH}}\boldsymbol{\omega}_{\mathtt{I},\mathtt{B}}} \times \underbrace{{}^{\mathtt{SH}}\boldsymbol{\omega}_{\mathtt{I},\mathtt{SH}}}_{{}^{\mathtt{SH}}\boldsymbol{\omega}_{\mathtt{I},\mathtt{B}}} \times {}^{\mathtt{SH}}\boldsymbol{r}_{o_{\mathtt{B}},o_{\mathtt{SH}}}, \tag{38} $$

and

$$ {}^{\mathtt{SM}}_{\mathtt{I},\mathtt{I}}\ddot{\boldsymbol{r}}_{o_{\mathtt{SH}},o_{\mathtt{SM}}} = \cancelto{\boldsymbol{0}}{{}^{\mathtt{SM}}_{\mathtt{SM},\mathtt{SM}}\ddot{\boldsymbol{r}}_{o_{\mathtt{SH}},o_{\mathtt{SM}}}} + {}^{\mathtt{SM}}\boldsymbol{\alpha}_{\mathtt{I},\mathtt{SM}} \times {}^{\mathtt{SM}}\boldsymbol{r}_{o_{\mathtt{SH}},o_{\mathtt{SM}}} + 2{}^{\mathtt{SM}}\boldsymbol{\omega}_{\mathtt{I},\mathtt{SM}} \times \cancelto{\boldsymbol{0}}{{}^{\mathtt{SM}}_{\mathtt{SM}}\dot{\boldsymbol{r}}_{o_{\mathtt{SH}},o_{\mathtt{SM}}}} + {}^{\mathtt{SM}}\boldsymbol{\omega}_{\mathtt{I},\mathtt{SM}} \times {}^{\mathtt{SM}}\boldsymbol{\omega}_{\mathtt{I},\mathtt{SM}} \times {}^{\mathtt{SM}}\boldsymbol{r}_{o_{\mathtt{SH}},o_{\mathtt{SM}}}, \tag{39} $$

respectively.

After substituting Eqs. 38 and 39 into Eq. 30, the operation results into velocity

$$ {}^{\mathtt{B}}_{\mathtt{I}}\dot{\boldsymbol{r}}_{o_{\mathtt{B}},o_{\mathtt{SM}}} = {}^{\mathtt{B}}\boldsymbol{\omega}_{\mathtt{I},\mathtt{B}} \times {}^{\mathtt{B}}\boldsymbol{r}_{o_{\mathtt{B}},o_{\mathtt{SM}}} + {}^{\mathtt{B}}\boldsymbol{\omega}_{\mathtt{B},\mathtt{SM}} \times {}^{\mathtt{B}}\boldsymbol{r}_{o_{\mathtt{SH}},o_{\mathtt{SM}}}, \tag{40} $$

DOI: 10.13009/EUCASS2023-549

and after substituting Eqs. 38 and 39 into Eq. 31, it results into acceleration

$$ {}^{\mathtt{B}}_{\mathtt{I},\mathtt{I}}\ddot{\boldsymbol{r}}_{\mathtt{o_B},\mathtt{o_{SM}}} = {}^{\mathtt{B}}\boldsymbol{\alpha}_{\mathtt{I,B}} \times {}^{\mathtt{B}}\boldsymbol{r}_{\mathtt{o_B},\mathtt{o_{SM}}} + {}^{\mathtt{B}}\boldsymbol{\omega}_{\mathtt{I,B}} \times {}^{\mathtt{B}}\boldsymbol{\omega}_{\mathtt{I,B}} \times {}^{\mathtt{B}}\boldsymbol{r}_{\mathtt{o_B},\mathtt{o_{SM}}} + {}^{\mathtt{B}}\boldsymbol{\alpha}_{\mathtt{B,SM}} \times {}^{\mathtt{B}}\boldsymbol{r}_{\mathtt{o_{SH}},\mathtt{o_{SM}}} + {}^{\mathtt{B}}\boldsymbol{\omega}_{\mathtt{B,SM}} \times {}^{\mathtt{B}}\boldsymbol{\omega}_{\mathtt{B,SM}} \times {}^{\mathtt{B}}\boldsymbol{r}_{\mathtt{o_{SH}},\mathtt{o_{SM}}} . \tag{41} $$

After performing the corresponding simplifications for planar flight, the velocity of the i-th sloshing mass for the pitch plane is defined in B-frame coordinates

$$ {}^{\mathtt{B}}_{\mathtt{I}}\dot{\boldsymbol{r}}_{\mathtt{o_B},\mathtt{o_{SM}}} = \begin{bmatrix} \left(\dot\theta + \dot\theta_{\mathrm{SM}}\right)\ell_{\mathrm{SM}} \sin\theta_{\mathrm{SM}} + \dot\theta \ell_{\mathrm{SH}} \sin\theta_{\mathrm{SH}} \\ 0 \\ \left(\dot\theta + \dot\theta_{\mathrm{SM}}\right)\ell_{\mathrm{SM}} \cos\theta_{\mathrm{SM}} - \dot\theta \ell_{\mathrm{SH}} \cos\theta_{\mathrm{SH}} \end{bmatrix}, \tag{42} $$

and the acceleration

$$ {}^{\mathtt{B}}_{\mathtt{I},\mathtt{I}}\ddot{\boldsymbol{r}}_{\mathtt{o_B},\mathtt{o_{SM}}} = \begin{bmatrix} \left(\ddot\theta + \ddot\theta_{\mathrm{SM}}\right)\ell_{\mathrm{SM}} \sin\theta_{\mathrm{SM}} + \left(\dot\theta + \dot\theta_{\mathrm{SM}}\right)^2 \ell_{\mathrm{SM}} \cos\theta_{\mathrm{SM}} + \ddot\theta \ell_{\mathrm{SH}} \sin\theta_{\mathrm{SH}} - \dot\theta^2 \ell_{\mathrm{SH}} \cos\theta_{\mathrm{SH}} \\ 0 \\ \left(\ddot\theta + \ddot\theta_{\mathrm{SM}}\right)\ell_{\mathrm{SM}} \cos\theta_{\mathrm{SM}} - \left(\dot\theta + \dot\theta_{\mathrm{SM}}\right)^2 \ell_{\mathrm{SM}} \sin\theta_{\mathrm{SM}} - \ddot\theta \ell_{\mathrm{SH}} \cos\theta_{\mathrm{SH}} - \dot\theta^2 \ell_{\mathrm{SH}} \sin\theta_{\mathrm{SH}} \end{bmatrix}. \tag{43} $$

2.3 Newton-Euler dynamics

For a system with multiple pendula, the derivation of equations can become quite complicated when performed analytically. In this part, we focus on obtaining the equations for a single pendulum connected to the rigid body, and later the analysis can be extended to cover a system with multiple bodies. The iterative Newton-Euler method[16,28,31] has seen success in the multibody dynamics and robotics fields,[17,29] where it is used to compute the EoMs of kinematic chains of systems with three-like structures. In other words, it can be easily applied to our problem[vii], which leads to a representative model that can be effortlessly implemented in simulation environment (e.g., Simulink®). In Fig. 4 we depict the simplest configuration for a RLV, with one tank and one sloshing mode, the pendulum is attached to the vehicle at the hinge point $o_{\mathtt{SH}}$. The equations that govern the interaction between the bodies are

$$ m_{\mathrm{B}}\, {}^{\mathtt{I}}\boldsymbol{a}_{\mathtt{o_E},\mathtt{o_B}} = {}^{\mathtt{I}}\boldsymbol{f}_{\mathrm{tot_B}} + {}^{\mathtt{I}}\boldsymbol{f}_{\mathrm{reac}} , \tag{44} $$

$$ m_i\, {}^{\mathtt{I}}\boldsymbol{a}_{\mathtt{o_E},\mathtt{o_{SM}}} = {}^{\mathtt{I}}\boldsymbol{f}_{\mathrm{tot_{SM}}} - {}^{\mathtt{I}}\boldsymbol{f}_{\mathrm{reac}} , \tag{45} $$

$$ {}^{\mathtt{I}}\boldsymbol{J}_{\mathrm{B}}\, {}^{\mathtt{I}}\boldsymbol{\alpha}_{\mathtt{I,B}} = {}^{\mathtt{I}}\boldsymbol{\tau}_{\mathrm{tot_B}} + {}^{\mathtt{I}}\boldsymbol{\tau}_{\mathrm{reac}} + {}^{\mathtt{I}}\boldsymbol{r}_{\mathtt{o_B},\mathtt{o_{SH}}} \times {}^{\mathtt{I}}\boldsymbol{f}_{\mathrm{reac}} , \tag{46} $$

$$ {}^{\mathtt{I}}\boldsymbol{J}_{\mathrm{m}_i}\, {}^{\mathtt{I}}\boldsymbol{\alpha}_{\mathtt{I,SM}} = {}^{\mathtt{I}}\boldsymbol{\tau}_{\mathrm{tot_{SM}}} - {}^{\mathtt{I}}\boldsymbol{\tau}_{\mathrm{reac}} - {}^{\mathtt{I}}\boldsymbol{r}_{\mathtt{o_{SM}},\mathtt{o_{SH}}} \times {}^{\mathtt{I}}\boldsymbol{f}_{\mathrm{reac}} , \tag{47} $$

where 44 and 45 describe the rigid body motion and 45 and 47 correspond to the pendulum translational and rotational motion. Although Eqs. 44-47 are expressed in inertial coordinates, the frame of reference can be easily changed to B- or SM-frame for a simpler representation of the EoMs.

The total (sum) forces and torques acting on each separated body are defined as follows[viii]

$$ {}^{\square}\boldsymbol{f}_{\mathrm{tot_B}} = m_{\mathrm{B}}\, {}^{\square}\boldsymbol{g} + {}^{\square}\boldsymbol{f}_{\mathrm{aero}} + {}^{\square}\boldsymbol{f}_{\mathrm{tvc}} , \tag{48} $$

$$ {}^{\square}\boldsymbol{f}_{\mathrm{tot_{SM}}} = m_i\, {}^{\square}\boldsymbol{g} , \tag{49} $$

$$ {}^{\square}\boldsymbol{\tau}_{\mathrm{tot_B}} = {}^{\square}\boldsymbol{\tau}_{\mathrm{damp_B}} + {}^{\square}\boldsymbol{\tau}_{\mathrm{aero}} + {}^{\square}\boldsymbol{\tau}_{\mathrm{tvc}} + {}^{\square}\boldsymbol{\tau}_{\mathrm{rcs}} , \tag{50} $$

$$ {}^{\square}\boldsymbol{\tau}_{\mathrm{tot_{SM}}} = {}^{\square}\boldsymbol{\tau}_{\mathrm{damp_{SM}}} . \tag{51} $$

The reaction force and torque are written as

$$ {}^{\square}\boldsymbol{f}_{\mathrm{reac}} = -m_i\, {}^{\square}\boldsymbol{a}_{\mathtt{o_E},\mathtt{o_{SM}}} + {}^{\square}\boldsymbol{f}_{\mathrm{tot_{SM}}} , \tag{52} $$

$$ \begin{aligned} {}^{\square}\boldsymbol{\tau}_{\mathrm{reac}} &= -{}^{\square}\boldsymbol{J}_{\mathrm{m}_i}\, {}^{\square}\boldsymbol{\alpha}_{\mathtt{I,SM}} + {}^{\square}\boldsymbol{\tau}_{\mathrm{tot_{SM}}} - {}^{\square}\boldsymbol{r}_{\mathtt{o_{SM}},\mathtt{o_{SH}}} \times {}^{\square}\boldsymbol{f}_{\mathrm{reac}} , \\ &= -{}^{\square}\boldsymbol{J}_{\mathrm{m}_i}\, {}^{\square}\boldsymbol{\alpha}_{\mathtt{I,SM}} + {}^{\square}\boldsymbol{\tau}_{\mathrm{tot_{SM}}} - {}^{\square}\boldsymbol{r}_{\mathtt{o_{SM}},\mathtt{o_{SH}}} \times \left(-m_i\, {}^{\square}\boldsymbol{a}_{\mathtt{o_E},\mathtt{o_{SM}}} + {}^{\square}\boldsymbol{f}_{\mathrm{tot_{SM}}}\right). \end{aligned} \tag{53} $$

Since we are mostly interested on the effect of the sloshing mass onto the rigid body, the translational dynamics of the pendulum was embedded into the rigid body dynamics (Eq. 44) via the reaction force (Eq. 52) at the hinge point, that is, expressing the dynamics directly in B-coordinates

$$ m_{\mathrm{B}}\, {}^{\mathtt{B}}_{\mathtt{I}}\ddot{\boldsymbol{r}}_{\mathtt{o_E},\mathtt{o_B}} = {}^{\mathtt{B}}\boldsymbol{f}_{\mathrm{tot_B}} - m_i\, {}^{\mathtt{B}}\boldsymbol{a}_{\mathtt{o_E},\mathtt{o_{SM}}} + {}^{\mathtt{B}}\boldsymbol{f}_{\mathrm{tot_{SM}}} , \tag{54} $$

[vii] This model can also be used for the calculation of engine induced oscillations (Tail-Wag-Dog) with the proper modifications to account for the position of the engine relative to the CoM of the vehicle.

[viii] The empty box super-index indicates that those vector can be expressed in any frame, e.g., I-, B-, SM-, or SH-frame by making use of the correct rotation matrix $\boldsymbol{\mathcal{R}}$.

DOI: 10.13009/EUCASS2023-549

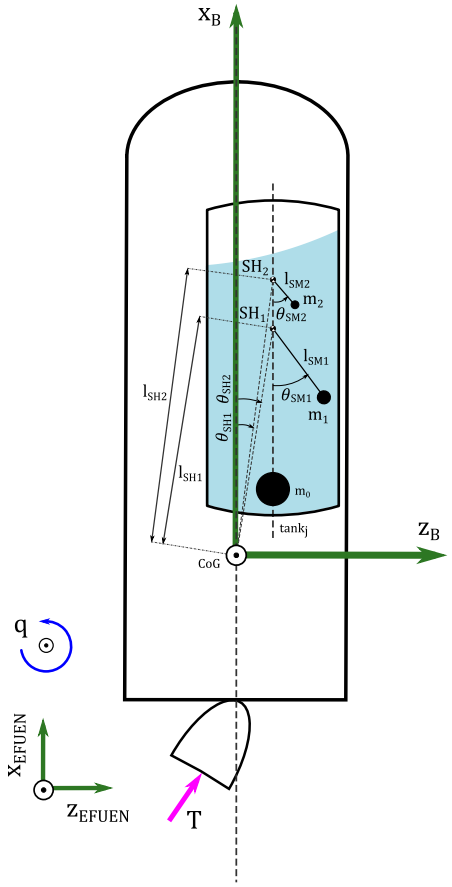

Figure 4: Principal sloshing frames.

and after performing further simplifications

$$\left(m_{\mathrm{B}}+m_i\right){}^{\mathtt{B}}_{\mathtt{I}}\ddot{\boldsymbol{r}}_{\mathtt{O_E},\mathtt{O_B}} = {}^{\mathtt{B}}\boldsymbol{f}_{\mathrm{tot_B}} + {}^{\mathtt{B}}\boldsymbol{f}_{\mathrm{tot_{SM}}} - m_i\,{}^{\mathtt{B}}_{\mathtt{I},\mathtt{I}}\boldsymbol{a}_{\mathtt{O_B},\mathtt{O_{SM}}}\,, \tag{55}$$

$$\left(m_{\mathrm{B}}+m_i\right){}^{\mathtt{B}}_{\mathtt{I}}\ddot{\boldsymbol{r}}_{\mathtt{O_E},\mathtt{O_B}} = \underbrace{m_{\mathrm{B}}\,{}^{\mathtt{B}}\boldsymbol{g} + {}^{\mathtt{B}}\boldsymbol{f}_{\mathrm{aero}} + {}^{\mathtt{B}}\boldsymbol{f}_{\mathrm{tvc}}}_{{}^{\mathtt{B}}\boldsymbol{f}_{\mathrm{tot_B}}} + \underbrace{m_i\,{}^{\mathtt{B}}\boldsymbol{g}}_{{}^{\mathtt{B}}\boldsymbol{f}_{\mathrm{tot_{SM}}}} - m_i\,{}^{\mathtt{B}}_{\mathtt{I},\mathtt{I}}\boldsymbol{a}_{\mathtt{O_B},\mathtt{O_{SM}}}\,, \tag{56}$$

$$\underbrace{\left(m_{\mathrm{B}}+m_i\right)}_{m_{\mathrm{tot}}}{}^{\mathtt{B}}_{\mathtt{I}}\ddot{\boldsymbol{r}}_{\mathtt{O_E},\mathtt{O_B}} = \underbrace{\left(m_{\mathrm{B}}+m_i\right)}_{m_{\mathrm{tot}}}{}^{\mathtt{B}}\boldsymbol{g} + {}^{\mathtt{B}}\boldsymbol{f}_{\mathrm{aero}} + {}^{\mathtt{B}}\boldsymbol{f}_{\mathrm{tvc}} \underbrace{-m_i\,{}^{\mathtt{B}}_{\mathtt{I},\mathtt{I}}\boldsymbol{a}_{\mathtt{O_B},\mathtt{O_{SM}}}}_{{}^{\mathtt{B}}\boldsymbol{f}_{\mathrm{slosh_B}}}\,, \tag{57}$$

and recalling that the inertial acceleration in body coordinates needs to be re-written as a function of Eq. 29, the sloshing force is thus rewritten as

$${}^{\square}\boldsymbol{f}_{\mathrm{slosh_B}} = -m_i\,{}^{\square}_{\mathtt{I},\mathtt{I}}\boldsymbol{a}_{\mathtt{O_B},\mathtt{O_{SM}}}\,. \tag{58}$$

Which for the planar case is expanded in B-coordinates to

$${}^{\mathtt{B}}\boldsymbol{f}_{\mathrm{slosh_B}} = m_i \begin{bmatrix} -\left(\ddot{\theta}+\ddot{\theta}_{\mathrm{SM}}\right)\ell_{\mathrm{SM}}\sin\theta_{\mathrm{SM}} - \left(\dot{\theta}+\dot{\theta}_{\mathrm{SM}}\right)^2\ell_{\mathrm{SM}}\cos\theta_{\mathrm{SM}} + \dot{\theta}^2\ell_{\mathrm{SH}} \\ 0 \\ -\left(\ddot{\theta}+\ddot{\theta}_{\mathrm{SM}}\right)\ell_{\mathrm{SM}}\cos\theta_{\mathrm{SM}} + \left(\dot{\theta}+\dot{\theta}_{\mathrm{SM}}\right)^2\ell_{\mathrm{SM}}\sin\theta_{\mathrm{SM}} + \ddot{\theta}\ell_{\mathrm{SH}} \end{bmatrix}. \tag{59}$$

The damping torque has a different sign depending on whether it is seen at the rigid body or at the pendulum arm. When analyzed from the rigid body perspective, it has the opposite direction to the angular velocity vector ${}^{\mathtt{B}}\boldsymbol{\omega}_{\mathtt{B,SM}}$. When seen at the pendulum's arm, the torque has the same direction as the angular velocity vector, i.e.,

$${}^{\square}\boldsymbol{\tau}_{\mathrm{damp_B}} = -{}^{\square}\boldsymbol{\tau}_{\mathrm{damp_{SM}}} = c_{\mathrm{SM}}\,{}^{\square}\boldsymbol{\omega}_{\mathtt{B,SM}}\,, \tag{60}$$

DOI: 10.13009/EUCASS2023-549

which could also be embedded into the EoMs as a force[ix]

$$ {}^{\mathtt{SM}}\boldsymbol{f}_{\mathrm{damp_{SM}}} = \left[{}^{\mathtt{SM}}\boldsymbol{r}_{\mathtt{o_{SM},o_{SH}}}\times\right]^{-1}\,{}^{\mathtt{SM}}\boldsymbol{\tau}_{\mathrm{damp_{SM}}} \approx \begin{bmatrix} 0 & 0 & -\frac{c_{\mathrm{SM}}\dot{\theta}_{\mathrm{SM}}}{\ell_{\mathrm{SM}}} \end{bmatrix}^{\top}, \tag{61} $$

and the simplified version in B-coordinates as seen from the rigid body perspective

$$ {}^{\mathtt{B}}\boldsymbol{f}_{\mathrm{damp_B}} = {}^{\mathtt{B}}\boldsymbol{\mathcal{R}}_{\mathtt{SH}}\left[{}^{\mathtt{SH}}\boldsymbol{r}_{\mathtt{o_B,o_{SH}}}\times\right]^{-1}\,{}^{\mathtt{SH}}\boldsymbol{\tau}_{\mathrm{damp_B}} \approx \begin{bmatrix} 0 & 0 & \frac{c_{\mathrm{SM}}\dot{\theta}_{\mathrm{SM}}}{\ell_{\mathrm{SH}}} \end{bmatrix}^{\top}. \tag{62} $$

For what regards the attitude dynamics of the multibody arrangement, the rotational dynamics of the pendulum is embedded into the rigid body (Eq. 46) by means of the reaction torque (Eq. 53) and the reaction force (Eq. 52). The first step is to eliminate the pendulum's MoI for the reasons explained in Sec. 1, this approach is consistent with the methodology from other authors.[23,24,35] Secondly, since we are mostly interested in the dynamics of the vehicle in the B-frame, the MoI must be also expressed in B-coordinates via the following relationship[x]

$$ {}^{\mathtt{I}}\boldsymbol{J}_{\mathrm{tot}}\,{}^{\mathtt{I}}_{\mathtt{I}}\boldsymbol{\alpha}_{\mathtt{I,B}} = {}^{\mathtt{B}}\boldsymbol{J}\,{}^{\mathtt{B}}_{\mathtt{B}}\boldsymbol{\alpha}_{\mathtt{I,B}} + {}^{\mathtt{B}}\boldsymbol{\omega}_{\mathtt{I,B}}\times\left({}^{\mathtt{B}}\boldsymbol{J}\,{}^{\mathtt{B}}\boldsymbol{\omega}_{\mathtt{I,B}}\right), \tag{63} $$

and so yielding

$$ \begin{aligned} {}^{\mathtt{B}}\boldsymbol{J}_{\mathrm{tot}}\,{}^{\mathtt{B}}\boldsymbol{\alpha}_{\mathtt{I,B}} + {}^{\mathtt{B}}\boldsymbol{\omega}_{\mathtt{I,B}}\times\left({}^{\mathtt{B}}\boldsymbol{J}_{\mathrm{tot}}\,{}^{\mathtt{B}}\boldsymbol{\omega}_{\mathtt{I,B}}\right) &= {}^{\mathtt{B}}\boldsymbol{\tau}_{\mathrm{tot_B}} + {}^{\mathtt{B}}\boldsymbol{\tau}_{\mathrm{react}} + {}^{\mathtt{B}}\boldsymbol{r}_{\mathtt{o_B,o_{SH}}}\times{}^{\mathtt{B}}\boldsymbol{f}_{\mathrm{react}}, && (64)\\ &= {}^{\mathtt{B}}\boldsymbol{\tau}_{\mathrm{tot_B}} + {}^{\mathtt{B}}\boldsymbol{\tau}_{\mathrm{tot_{SM}}} + {}^{\mathtt{B}}\boldsymbol{r}_{\mathtt{o_B,o_{SM}}}\times\left(-m_i\,{}^{\mathtt{B}}_{\mathtt{I,I}}\boldsymbol{a}_{\mathtt{o_E,o_{SM}}} + {}^{\mathtt{B}}\boldsymbol{f}_{\mathrm{tot_{SM}}}\right), && (65)\\ &= {}^{\mathtt{B}}\boldsymbol{\tau}_{\mathrm{tot_B}} + {}^{\mathtt{B}}\boldsymbol{\tau}_{\mathrm{tot_{SM}}} + {}^{\mathtt{B}}\boldsymbol{r}_{\mathtt{o_B,o_{SM}}}\times\left(-m_i\,{}^{\mathtt{B}}_{\mathtt{I,I}}\boldsymbol{a}_{\mathtt{o_E,o_{SM}}} + {}^{\mathtt{B}}\boldsymbol{f}_{\mathrm{tot_{SM}}}\right), && (66)\\ &= {}^{\mathtt{B}}\boldsymbol{\tau}_{\mathrm{aero}} + {}^{\mathtt{B}}\boldsymbol{\tau}_{\mathrm{rcs}} + {}^{\mathtt{B}}\boldsymbol{\tau}_{\mathrm{tvc}} + \underbrace{{}^{\mathtt{B}}\boldsymbol{\tau}_{\mathrm{damp_{SM}}} - m_i\,{}^{\mathtt{B}}\boldsymbol{r}_{\mathtt{o_B,o_{SM}}}\times\left({}^{\mathtt{B}}_{\mathtt{I,I}}\boldsymbol{a}_{\mathtt{o_E,o_{SM}}} - {}^{\mathtt{B}}\boldsymbol{g}\right)}_{{}^{\mathtt{B}}\boldsymbol{\tau}_{\mathrm{slosh_B}}}. && (67) \end{aligned} $$

Therefore, the sloshing torque is defined as

$$ {}^{\mathtt{B}}\boldsymbol{\tau}_{\mathrm{slosh_B}} = -m_i\,{}^{\mathtt{B}}\boldsymbol{r}_{\mathtt{o_B,o_{SM}}}\times\left({}^{\mathtt{I}}\boldsymbol{a}_{\mathtt{o_E,o_{SM}}} - {}^{\mathtt{B}}\boldsymbol{g}\right) + {}^{\mathtt{B}}\boldsymbol{\tau}_{\mathrm{damp_{SM}}}, \tag{68} $$

which for the planar case can be expressed as ${}^{\mathtt{B}}\boldsymbol{\tau}_{\mathrm{slosh_B}} = \begin{bmatrix} 0 & \tau_{\mathrm{y_{slosh_B}}} & 0 \end{bmatrix}^{\top}$, i.e.,

$$ \tau_{\mathrm{y_{slosh_B}}} = -m_i\Big[\Big(\Gamma + {}^{\mathtt{B}}_{\mathtt{I,I}}\ddot{\mathtt{x}}_{\mathtt{o_B,o_{SM}}}\Big)\Big(\ell_{\mathrm{SH}}\sin\theta_{\mathrm{SH}} + \ell_{\mathrm{SM}}\sin\theta_{\mathrm{SM}}\Big) - {}^{\mathtt{B}}_{\mathtt{I,I}}\ddot{\mathtt{z}}_{\mathtt{o_B,o_{SM}}}\Big(\ell_{\mathrm{SH}}\cos\theta_{\mathrm{SH}} - \ell_{\mathrm{SM}}\cos\theta_{\mathrm{SM}}\Big)\Big] - c_{\mathrm{SM}}\,{}^{\mathtt{B}}\boldsymbol{\omega}_{\mathtt{B,SM}}, \tag{69} $$

The computation of the EoMs of the pendulum is a simpler process. The mass and pendulum arm are assumed to be decoupled from the rigid body. For the position dynamics, one takes Eq. 45 and makes the reaction force equal to zero, which produces

$$ m_i\Big({}^{\mathtt{SM}}_{\mathtt{I,I}}\ddot{\boldsymbol{r}}_{\mathtt{o_E,o_{SM}}} - {}^{\mathtt{SM}}g\Big) = \boldsymbol{0}. \tag{70} $$

The same assumptions hold for the rotational dynamics. In this case, Eq. 47 is reduced by dropping the effect of the reaction torque, but not the one of the reaction force

$$ -m_i\,{}^{\mathtt{SM}}\boldsymbol{r}_{\mathtt{o_{SM},o_{SH}}}\times\left({}^{\mathtt{SM}}_{\mathtt{I,I}}\ddot{\boldsymbol{r}}_{\mathtt{o_E,o_{SM}}} - {}^{\mathtt{SM}}\boldsymbol{g}\right) = \boldsymbol{0}. \tag{71} $$

It is not necessary to include both position and rotation of the pendulum, for the calculation of the linearized state space model, either of them suffices. Some authors prefer the inclusion of the lateral effects,[23] while in this presentation we focus on the rotation dynamics to take advantage of the modeling framework. For the planar case, and assuming a tank along the longitudinal axis, Eq. 71 can be further reduced to

$$ \begin{aligned} m_i\,{}^{\mathtt{B}}_{\mathtt{I,I}}\ddot{\mathtt{x}}_{\mathtt{o_E,o_B}}\ell_{\mathrm{SM}}\sin\theta_{\mathrm{SM}} + m_i\,{}^{\mathtt{B}}_{\mathtt{I,I}}\ddot{\mathtt{z}}_{\mathtt{o_E,o_B}}\ell_{\mathrm{SM}}\cos\theta_{\mathrm{SM}} + m_i\Big(\ddot{\theta} + \ddot{\theta}_{\mathrm{SM}}\Big)\ell_{\mathrm{SM}}{}^2 + m_i g\ell_{\mathrm{SM}}\sin\Big(\theta + \theta_{\mathrm{SM}}\Big)\\ -m_i\,\ddot{\theta}\ell_{\mathrm{SH}}\ell_{\mathrm{SM}}\cos\theta_{\mathrm{SM}} - m_i\,\dot{\theta}^2\ell_{\mathrm{SH}}\ell_{\mathrm{SM}}\sin\theta_{\mathrm{SM}} + c_{\mathrm{SM}}\dot{\theta}_{\mathrm{SM}} = 0. \end{aligned} \tag{72} $$

[ix] The inverse of the cross-product operation is not uniquely defined, i.e., there are many combinations of skew symmetric position matrix that pre-multiplied by the torque produce the target force vector. However, for the case where two of position vector components are zero, the solution becomes defined and can be easily computed.

[x] For the frame transformation of the MoI, one must pre- and post-multiply by the rotation matrix and its transpose, i.e., ${}^{\mathtt{B}}\boldsymbol{J}_{\mathrm{tot}} = {}^{\mathtt{B}}\boldsymbol{\mathcal{R}}_{\mathtt{I}}\,{}^{\mathtt{I}}\boldsymbol{J}_{\mathrm{tot}}\,{}^{\mathtt{B}}\boldsymbol{\mathcal{R}}_{\mathtt{I}}{}^{\top}$.

DOI: 10.13009/EUCASS2023-549

2.4 Summary of the equations

For the sake of simplicity, we group Eqs. 57, 67, 70 and 71 here below[xi,xii]

$$m_{\text{tot}}\,{}^{\text{B}}_{\text{I,I}}\ddot{\boldsymbol{r}}_{\text{O}_\text{E},\text{O}_\text{B}} = m_{\text{tot}}\,{}^{\text{B}}\boldsymbol{g} + {}^{\text{B}}\boldsymbol{f}_{\text{aero}} + {}^{\text{B}}\boldsymbol{f}_{\text{tvc}} \underbrace{-m_i\,{}^{\text{B}}_{\text{I,I}}\ddot{\boldsymbol{r}}_{\text{O}_\text{B},\text{O}_\text{SM}}}_{{}^{\text{B}}\boldsymbol{f}_{\text{slosh}}}, \tag{57}$$

$${}^{\text{B}}\boldsymbol{J}\,{}^{\text{B}}\boldsymbol{\alpha}_{\text{I,B}} + {}^{\text{B}}\boldsymbol{\omega}_{\text{I,B}} \times \left({}^{\text{B}}\boldsymbol{J}\,{}^{\text{B}}\boldsymbol{\omega}_{\text{I,B}}\right) = {}^{\text{B}}\boldsymbol{\tau}_{\text{aero}} + {}^{\text{B}}\boldsymbol{\tau}_{\text{rcs}} + {}^{\text{B}}\boldsymbol{\tau}_{\text{tvc}} \underbrace{-m_i\,{}^{\text{B}}\boldsymbol{r}_{\text{O}_\text{B},\text{O}_\text{SM}} \times \left({}^{\text{B}}_{\text{I,I}}\ddot{\boldsymbol{r}}_{\text{O}_\text{E},\text{O}_\text{SM}} - {}^{\text{B}}\boldsymbol{g}\right)}_{{}^{\text{B}}\boldsymbol{\tau}_{\text{slosh}_\text{B}}}, \tag{67}$$

$$0 = m_i\left({}^{\text{SM}}_{\text{I,I}}\ddot{\boldsymbol{r}}_{\text{O}_\text{E},\text{O}_\text{SM}} - {}^{\text{SM}}\boldsymbol{g}\right), \tag{70}$$

$$0 = m_i\,{}^{\text{SM}}\boldsymbol{r}_{\text{O}_\text{SM},\text{O}_\text{SH}} \times \left({}^{\text{SM}}_{\text{I,I}}\ddot{\boldsymbol{r}}_{\text{O}_\text{E},\text{O}_\text{SM}} - {}^{\text{SM}}\boldsymbol{g}\right) - {}^{\text{SM}}\boldsymbol{\tau}_{\text{damp}_\text{SM}}, \tag{71}$$

indeed these definitions can be implemented directly in a 6-DoF simulation environment. This is the core reason behind choosing the iterative iterative Newton-Euler for the derivation of the model; it can be easily converted into code for numerical simulations. The pendulum model can be also seen as an add-on block to an already existing full rigid body simulation, i.e., only ${}^{\text{B}}\boldsymbol{f}_{\text{slosh}}$, ${}^{\text{B}}\boldsymbol{\tau}_{\text{slosh}}$ and Eq. 71 form the missing building block. We highlight the fact that the equation's validation has been carried out wrt. a more standardized approach; the Lagrangian formulation, which is also included in the *Symbolic Multibody Dynamics* toolbox. Furthermore, we prepare the ground for an ongoing study, where we compare and validate our models to one from a model-oriented approach[10] using the Modelica language.

2.5 Linearization

For the linearization of the EoMs we concentrate in Eqs. 57, 67, and 71. There are some important steps that were omitted here to contain the size of this publication:

1. Substitute the translational and rotation quantities presented across Secs. 2.1 and 2.2.
2. Since we are mostly interested in the pitch-directional motion, but the model for the yaw-lateral motion will be equivalent, we assume planar flight, and hence, temporarily disregard the yaw-lateral motion.
3. Since the vehicle is assumed to be flying a gravity turn trajectory, small perturbations about the reference solution are used.
4. All trim angles are assumed to be small, thus trigonometric functions can be simplified ($\sin a \approx a$ and $\cos a \approx 1$).
5. The product of two small elements is assumed to be zero ($ab \approx 0$).
6. The longitudinal non-gravitational acceleration has been compressed into element Γ.
7. If one performs the simplifications and looks at the resulting model for the coupled longitudinal axis, the effect of the sloshing mass onto the rigid body vanishes.
8. The damping coefficient was substituted as $c_{\text{SM}} = 2\zeta_{\text{SM}}\sqrt{\Gamma\ell_{\text{SM}}}$, where ζ_{SM} represents the true damping coefficient defined for the given tank geometry an characteristics, it is also affected by the existence baffles or assumed to be zero when no value is provided.

The set of non-linear simplified equations is denoted by

$$m_i\left(\ell_{\text{SM}} - \ell_{\text{SH}}\right)\ddot{\theta} + \left(m_\text{B} + m_i\right)\Gamma\theta + \left(m_\text{B} + m_i\right){}^{\text{B}}\ddot{\text{z}} + m_i\ell_{\text{SM}}\ddot{\theta}_{\text{SM}} = {}^{\text{B}}f_{\text{z}_\text{tvc}} + {}^{\text{B}}f_{\text{z}_\text{aero}}, \tag{73}$$

$$\left(J_{\text{yy}_\text{B}} + m_i\left(\ell_{\text{SM}} - \ell_{\text{SH}}\right)^2\right)\ddot{\theta} + m_i\Gamma\left(\ell_{\text{SM}} - \ell_{\text{SH}}\right)\theta + m_i\left(\ell_{\text{SM}} - \ell_{\text{SH}}\right){}^{\text{B}}\ddot{\text{z}} + m_i\ell_{\text{SM}}\left(\ell_{\text{SM}} - \ell_{\text{SH}}\right)\ddot{\theta}_{\text{SM}} + \Gamma m_i\ell_{\text{SM}}\theta_{\text{SM}} = {}^{\text{B}}\tau_{\text{y}_\text{tvc}} + {}^{\text{B}}\tau_{\text{y}_\text{aero}}, \tag{74}$$

$$\left(\ell_{\text{SM}} - \ell_{\text{SH}}\right)\ddot{\theta} + \Gamma\theta + {}^{\text{B}}\ddot{\text{z}} + \ell_{\text{SM}}\ddot{\theta}_{\text{SM}} + 2\zeta_{\text{SM}}\sqrt{\Gamma\ell_{\text{SM}}}\dot{\theta}_{\text{SM}} + \Gamma\theta_{\text{SM}} = 0. \tag{75}$$

[xi] An alternative formulation of the position dynamics equation is $m_\text{B}\,{}^{\text{B}}_{\text{I,I}}\ddot{\boldsymbol{r}}_{\text{O}_\text{E},\text{O}_\text{B}} = m_\text{B}\,{}^{\text{B}}\boldsymbol{g} + {}^{\text{B}}\boldsymbol{f}_{\text{aero}} + {}^{\text{B}}\boldsymbol{f}_{\text{tvc}} - m_i\left({}^{\text{B}}_{\text{I,I}}\ddot{\boldsymbol{r}}_{\text{O}_\text{E},\text{O}_\text{SM}} - {}^{\text{B}}\boldsymbol{g}\right)$.

[xii] The longitudinal component of the non-gravitational acceleration is defined as $\Gamma = \left(\text{T} - \mathcal{A}\right)/m_{\text{tot}} = {}^{\text{B}}_{\text{I,I}}\ddot{\text{x}}_{\text{O}_\text{E},\text{O}_\text{B}} + g\sin\theta$.

DOI: 10.13009/EUCASS2023-549

A key finding in Eq. 75 is the appearance of the harmonic oscillator corresponding to the pendulum dynamics, which is a second order system with a natural frequency equal to ${\omega_{\mathrm{n}}}^2 = \Gamma/\ell_{\mathrm{SM}}$.

For the computation of the state-space equations, the linearized aerodynamic forces and torque can be introduced to the linear equations as[21]

$$ {}^{\mathrm{B}}f_{\mathrm{x_{aero}}} = -X_\alpha\theta - X_{\dot{\mathrm{Z}}}\dot{\mathrm{z}} - X_{\delta_\theta}\delta_\theta + X_{\dot{\mathrm{z}}}v_{\mathrm{W}}\,, \tag{76} $$

$$ {}^{\mathrm{B}}f_{\mathrm{z_{aero}}} = -Z_\alpha\theta - X_{\dot{\mathrm{Z}}}\dot{\mathrm{z}} - Z_{\delta_\theta}\delta_\theta + Z_{\dot{\mathrm{z}}}v_{\mathrm{W}}\,, \tag{77} $$

$$ {}^{\mathrm{B}}\tau_{\mathrm{y_{aero}}} = \mu_\alpha\theta + \mu_{\dot{\mathrm{z}}}\dot{\mathrm{z}} + \mu_{\delta_\theta}\delta_\theta - \mu_{\dot{\mathrm{z}}}v_{\mathrm{W}}\,, \tag{78} $$

where δ_θ is the virtual fin deflection for the pitch channel. The linearized Thrust Vector Control (TVC) dynamics is written[21]

$$ {}^{\mathrm{B}}f_{\mathrm{x_{tvc}}} = -X_{\delta_y}\delta_y + X_{\mathrm{T}}\mathrm{T}\,, \tag{79} $$

$$ {}^{\mathrm{B}}f_{\mathrm{z_{tvc}}} = -Z_{\delta_y}\delta_y - Z_{\mathrm{T}}\mathrm{T}\,, \tag{80} $$

$$ {}^{\mathrm{B}}\tau_{\mathrm{y_{tvc}}} = -\mu_{\delta_y}\delta_y - \mu_{\mathrm{T}}\mathrm{T}\,, \tag{81} $$

δ_y is the pitch TVC deflection. The definition of the missing coefficients can be found in Macés-Hernández.[21] After rearranging Eqs. 73, 74 and 75 and later performing the derivatives wrt. the states vector $\boldsymbol{x} = \begin{bmatrix}\theta & \dot{\theta} & {}^{\mathrm{B}}\mathrm{Z} & {}^{\mathrm{B}}\dot{\mathrm{Z}} & \theta_{\mathrm{SM}} & \dot{\theta}_{\mathrm{SM}}\end{bmatrix}^\top$ and control inputs vector $\boldsymbol{u} = \begin{bmatrix}\delta_y & \delta_z\end{bmatrix}^\top$, the state space of the form $\boldsymbol{x} = \mathbf{A}\dot{\boldsymbol{x}} + \mathbf{B}\boldsymbol{u}$ is obtained

$$ \begin{bmatrix} \dot{\theta} \\ \ddot{\theta} \\ {}^{\mathrm{B}}\dot{\mathrm{Z}} \\ {}^{\mathrm{B}}\ddot{\mathrm{Z}} \\ \hline \dot{\theta}_{\mathrm{SM}} \\ \ddot{\theta}_{\mathrm{SM}} \end{bmatrix} = \left[\begin{array}{cccc|cc} 0 & 1 & 0 & 0 & 0 & 0 \\ \mu_\alpha & 0 & 0 & \mu_{\dot{\mathrm{z}}} & \mu_{\theta_{\mathrm{SM}}} & 0 \\ 0 & 0 & 0 & 1 & 0 & 0 \\ -\Gamma - Z_\alpha & 0 & 0 & -Z_{\dot{\mathrm{z}}} & Z_{\theta_{\mathrm{SM}}} & 0 \\ \hline 0 & 0 & 0 & 0 & 0 & 1 \\ \mu_{\ddot{\theta}_{\mathrm{SM}},\theta} & 0 & 0 & \mu_{\ddot{\theta}_{\mathrm{SM}},\dot{\mathrm{z}}} & \mu_{\ddot{\theta}_{\mathrm{SM}},\theta_{\mathrm{SM}}} & 0 \end{array}\right] \left[\begin{array}{c} \theta \\ \dot{\theta} \\ {}^{\mathrm{B}}\mathrm{Z} \\ {}^{\mathrm{B}}\dot{\mathrm{Z}} \\ \hline \theta_{\mathrm{SM}} \\ \dot{\theta}_{\mathrm{SM}} \end{array}\right] + \left[\begin{array}{cc} 0 & 0 \\ -\mu_{\delta_y} & \mu_{\delta_\theta} \\ 0 & 0 \\ -Z_{\delta_y} & -Z_{\delta_\theta} \\ \hline 0 & 0 \\ \mu_{\ddot{\theta}_{\mathrm{SM}},\delta_y} & \mu_{\ddot{\theta}_{\mathrm{SM}},\delta_\theta} \end{array}\right] \begin{bmatrix}\delta_y \\ \delta_\phi\end{bmatrix}, \tag{82} $$

with

$$ \mu_{\theta_{\mathrm{SM}}} = -\frac{\Gamma\ell_{\mathrm{SH}}m_i}{J_{\mathrm{yy}}}\,, \qquad Z_{\theta_{\mathrm{SM}}} = \frac{\Gamma m_i}{m_{\mathrm{B}}}\,, $$

$$ \mu_{\ddot{\theta}_{\mathrm{SM}},\theta} = \frac{1}{\ell_{\mathrm{SM}}}\left(Z_\alpha - \mu_\alpha\left(\ell_{\mathrm{SM}} - \ell_{\mathrm{SH}}\right)\right), \qquad \mu_{\ddot{\theta}_{\mathrm{SM}},\dot{\mathrm{z}}} = \frac{1}{\ell_{\mathrm{SM}}}\left(Z_{\dot{\mathrm{z}}} - \mu_{\dot{\mathrm{z}}}\left(\ell_{\mathrm{SM}} - \ell_{\mathrm{SH}}\right)\right). $$

$$ \mu_{\ddot{\theta}_{\mathrm{SM}},\theta_{\mathrm{SM}}} = \frac{\Gamma}{\ell_{\mathrm{SM}}}\left(\frac{J_{\mathrm{yy}}\left(m_{\mathrm{B}} + m_i\right) - m_i m_{\mathrm{B}}\ell_{\mathrm{SH}}\left(\ell_{\mathrm{SM}} - \ell_{\mathrm{SH}}\right)}{J_{\mathrm{yy}}m_{\mathrm{B}}}\right), $$

$$ \mu_{\ddot{\theta}_{\mathrm{SM}},\delta_y} = \frac{1}{\ell_{\mathrm{SM}}}\left(Z_{\delta_y} + \mu_{\delta_y}\left(\ell_{\mathrm{SM}} - \ell_{\mathrm{SH}}\right)\right), $$

$$ \mu_{\ddot{\theta}_{\mathrm{SM}},\delta_\theta} = \frac{1}{\ell_{\mathrm{SM}}}\left(Z_{\delta_\theta} + \mu_{\delta_\theta}\left(\ell_{\mathrm{SM}} - \ell_{\mathrm{SH}}\right)\right). $$

For all the combinations input-output, we are mostly interested in the attitude channels; $\theta(s)/\delta_y(s)$ and $\theta(s)/\delta_\theta(s)$. The resulting attitude transfer function can be expressed as[xiii]

$$ \frac{\theta}{\delta_i}(s) = \mathcal{G}_{\mathrm{rigid}}(s)\left(\frac{s^2 + {\omega_{\mathrm{z}_i}}^2}{s^2 + {\omega_{\mathrm{p}_i}}^2}\right) \tag{83} $$

for a system without damping coefficient, with

$$ {\omega_{\mathrm{z}_i}}^2 = \frac{\Gamma}{\ell_{\mathrm{SM}}}\left(\frac{\ell_\delta\left(m_{\mathrm{B}} + m_i\right) - \ell_{\mathrm{SH}}m_i}{\ell_\delta\, m_{\mathrm{B}}}\right), \qquad {\omega_{\mathrm{p}_i}}^2 = \frac{\Gamma}{\ell_{\mathrm{SM}}}\left(\frac{J_{\mathrm{yy_B}}\left(m_{\mathrm{B}} + m_i\right) - m_{\mathrm{B}}\, m_i\ell_{\mathrm{SH}}\left(\ell_{\mathrm{SM}} - \ell_{\mathrm{SH}}\right)}{J_{\mathrm{yy_B}}\, m_{\mathrm{B}}}\right). $$

It is interesting to look at the two frequencies that arise at the numerator and denominator, ω_{z_i} and ω_{p_i}. According to the findings of Pei,[23] which seem to be in line with classic references[11] in the field, in order for the sloshing mode to be phase stable, $\omega_{\mathrm{z}_i} < \omega_{\mathrm{p}_z}$ is required. When solving the inequality analytically, one might find that the position of the i-th sloshing mass must be below the denominated center of percussion $\ell_{\mathrm{perc}} = J_{\mathrm{yy}}/(\ell_\delta m_{\mathrm{B}})$. If the mass is between this point and the vehicle's Center of Gravity (CoG), the actuator can indirectly add energy to the mode when it has an

[xiii] For the TVC channel, the classic full order transfer function can for each output be derived from state-space model 82. The attitude channel is described by 1) $\mathcal{G}_{\mathrm{rigid}}(s) = -\left(\mu_{\delta_y}s + Z_{\dot{\mathrm{z}}}\mu_{\delta_y} + Z_{\delta_y}\mu_{\dot{\mathrm{z}}}\right)/\left(s^3 + Z_{\dot{\mathrm{z}}}s^2 - \mu_\alpha s + \left(Z_\alpha\mu_{\dot{\mathrm{z}}} - Z_{\dot{\mathrm{z}}}\mu_\alpha + \Gamma\mu_{\dot{\mathrm{z}}}\right)\right)$, which can be reduced to 2) $\mathcal{G}_{\mathrm{rigid}}(s) = -\mu_{\delta_y}/\left(s^2 - \mu_\alpha s\right)$, when assuming negligible contribution from the directional channel, and to 3) $\mathcal{G}_{\mathrm{rigid}}(s) = -\mu_{\delta_y}/s^2$ when there are no aerodynamic effects.

DOI: 10.13009/EUCASS2023-549

unfavorable phasing or it is phase unstable, thus propagating the instability to the rigid body. Recall the root-locus plot, if the trajectories from the pair of complex conjugate poles enter the complex conjugate pair of zeros on the right side of the complex plane, then the mode is unstable. A faster way of determining the stability of the modes is by evaluating the definition of the center of percussion directly onto the flight envelope and vehicle's characteristics.

3. Application to the CALLISTO mission

The details of the Cooperative Action Leading to Launcher Innovation for Stage Tossback Operation (CALLISTO) mission can be found in other references.[8,9,14,21,27] For the purposes of this publication, we characterize the behavior within its Liquid Oxygen (LOx) and LH_2: Liquid Hydrogen (LH2) tanks within the scope of the models presented across previous sections. Firstly, all the parameters presented in Tab. 1 were computed for the baseline vehicle architecture and mission profile, which is a classic Return-to-Launch-Site (RTLS) scenario trajectory, commonly found in RLVs. Secondly, the parameters were validated against the datasets from CFD computations[18,22] for the first mode of both tanks. During early design stages, the former were used, whereas the latter are the baseline for the flight tests. Those results are depicted in Fig. 4, we include relative positions, masses, and frequencies for the first mode. On the upper and lower subplots on the rightmost side, one observes that the desired CL attitude frequency is quite close to the frequency of both first modes, making the control design more challenging.

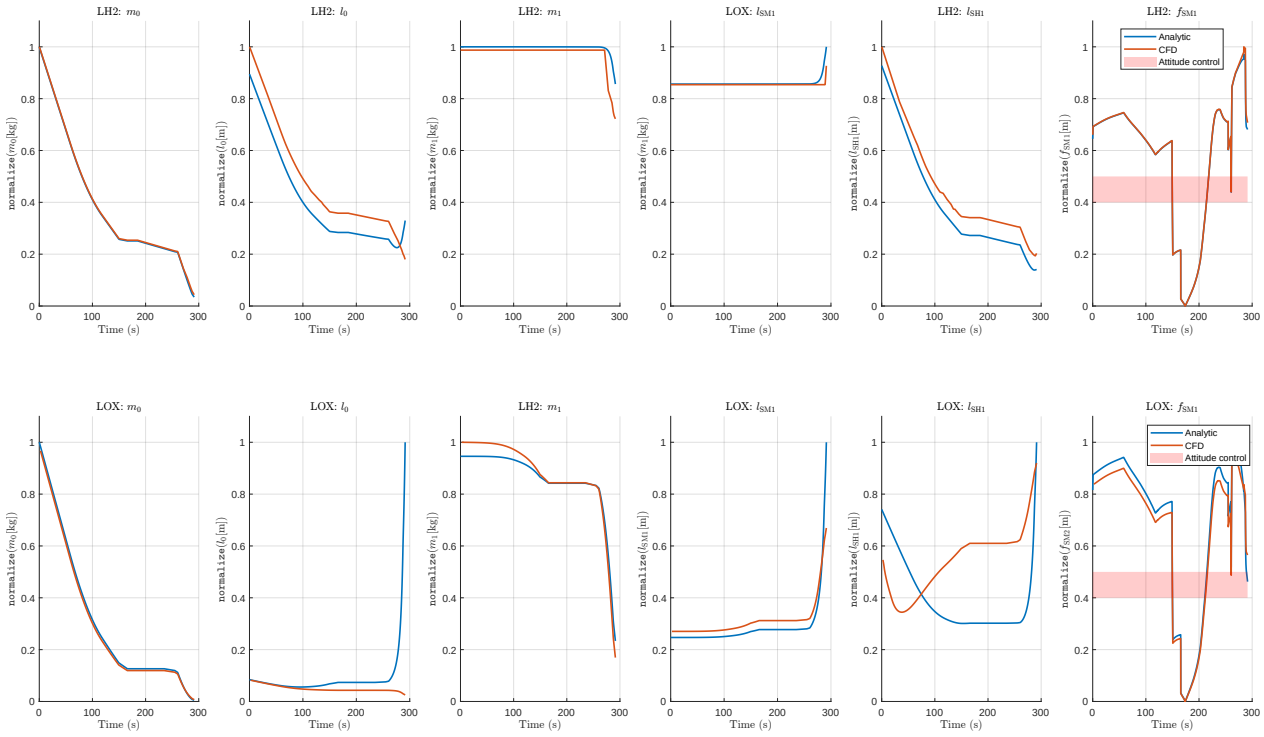

Figure 5: Comparison between the CFD data and analytical formulas.

Since the CALLISTO vehicle is actuated by commanding the TVC or the fins, there exist a center of percussion for each actuator. The evolution of the relative position of the masses for the entire mission is shown in Fig. 3, as well as the location of the CoM and the two corresponding danger zones. In our investigations we focus mostly on the ascent part of the mission,[27] this flight phase is done with FFO (fins Folded, legs Folded and thrust On) aerodynamic configuration, although UFO (fins Unfolded, legs Folded and thrust On) aerodynamic configuration is also an option, thus purely TVC actuated. We observe that the first mode's mass for the LOx tank crosses the TVC danger zone for few seconds at the beginning of the mission. Furthermore, the firsts mode's mass for the LH2 tank is always contained within the fin's danger zone. The crossings indicate that further analysis on the stability of the modes had to be performed. Since the design of the tanks can be only improved during early design phases, the study of several configuration for the inclusion of damping devices was took place[18,22] across the program.

The current vehicle design has converged to a point where the inclusion of the modes within the danger zones does not pose any risk for the mission, this means sufficient damping is guaranteed at all times. Furthermore, from

DOI: 10.13009/EUCASS2023-549

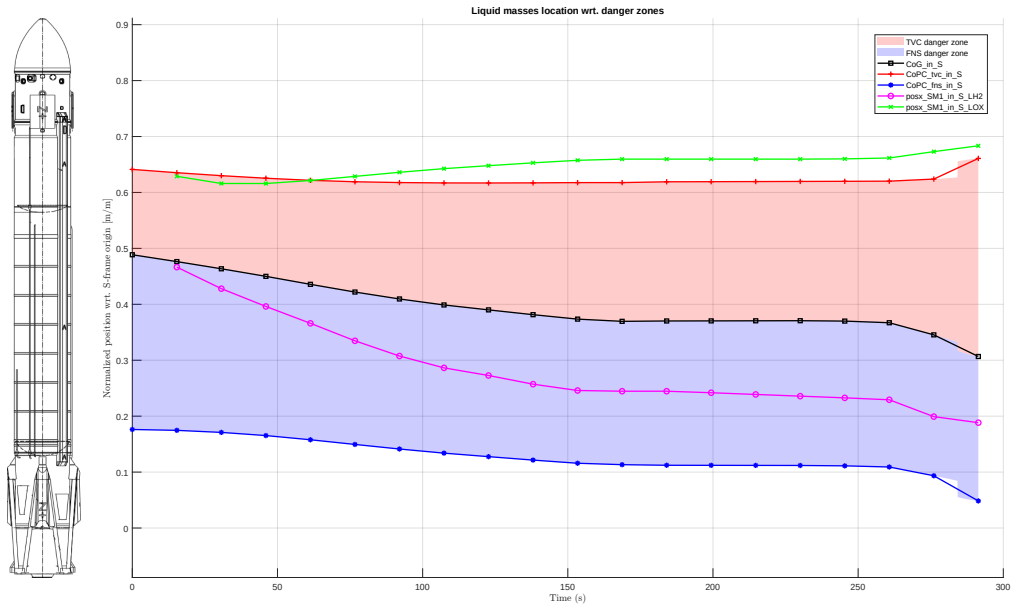

Figure 6: Relative position of the first mode masses relative to the danger zones.

GNC side, the design of the control system has been done in such a way that even if the modes are stable, the rigid body controller is not actively interacting with them.

One of the first design challenges was that direct filtering using anti-resonance filters was not possible due to the close proximity with the rigid body bandwidth, those filters can also degrade the rigid body control effectiveness. Decreasing the rigid body bandwidth too much also introduces performance degradation during trajectory tracking and wind disturbance minimization.

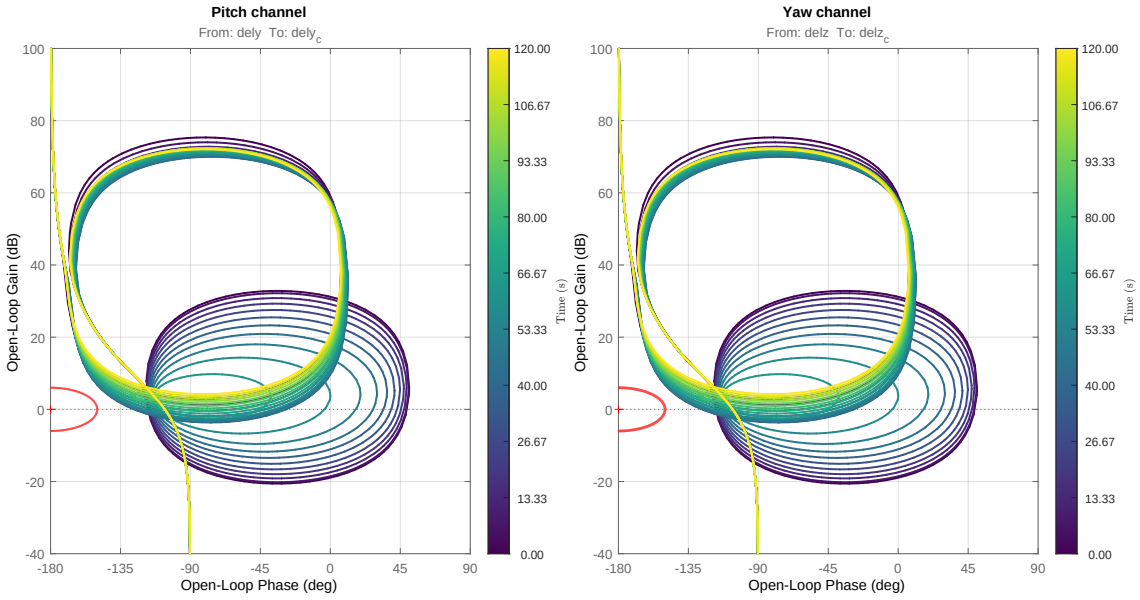

Figure 7: Nichols plot for attitude channel and two modes.

The advantage of using $\mathcal{H}_\infty$ methods for the computation of the control gains is that, the CL bandwidth can be directly imposed in the formulation of the control problem via the weight in the complementary sensitivity function, and adjusted accordingly for several conditions. In CALLISTO, we employ exploit those methods for the design of the control system. For a better overview on the control system for the mission, the reader is referred to our earlier works.[21,26] The key aspect differing from earlier design is that the state-space models used for control design no longer are the rigid body with aerodynamic effects, but rather those that also include the modes of LOx and LH2 tanks (i.e., Eq. 82). During our design process, several iterations have been necessary to converge to a satisfactory design. The

DOI: 10.13009/EUCASS2023-549

controllers synthesized for the baseline mission are presented in Fig. 7. Classic gain and phase margins were impose to account for uncertainties in the plant and sloshing parameters, and wind disturbances (6 dB and 30°). We highlight the fact that the nominal and robust stability margins were achieved for the full closed loop state-space model; however, in Fig. 7 we present only those of the decoupled attitude channel due to proprietary reasons.

4. Conclusion

In this paper, the modeling of the liquid behavior within the tanks of a liquid-propelled space vehicle has been explained. We tackled the modeling problem using an approach more oriented towards GNC analysis and design purposes. In the first part, we introduced a revision of the equations found in historical references and we made a summary of all the parameters that are needed for such performance analysis at early design phases and flight qualification.

The 3D model was derived using the Newton-Euler iterative method for multibody systems for a single mode, the tools needed for its extension to multiple tanks, multiple modes, and different tank positions relative to the CoM of the vehicle have been provided. We elaborated in the process of reducing the 3D equations to a planar simplification, and later, the computation of a state-space model for a generic RLV pitch plane. The simplifications for the different transfer function for the attitude channel was also introduced, here the user has the choice of selecting the full order with aerodynamic effects, the attitude decoupled one with aerodynamics of the simplest form decoupled attitude without aerodynamic effects.

In the final part, we applied all the models to the CALLISTO mission. The parameters summarized in Tab. 1 were computed for the vehicle and then validated against CFD simulations. The position of the sloshing masses was studied with regards to the danger zone for the baseline mission. As a consequence, the stability of the modes was carried out for the LOx and LH2 tanks. In the final part, the state-space model was used for the extension of our $\mathcal{H}_\infty$ synthesized controllers from previous investigations, where a proper imposition of the CL bandwidth allowed finding the middle ground between tracking performance and sufficient separation to the sloshing modes' frequencies, and at the same time it guaranteed a correct rejection of wind disturbances.

5. Acknowledgments

The authors of this paper would like thank the fruitful discussions with our colleagues from the GNC department of the DLR in Bremen, as well as our colleagues from other DLR institutes, JAXA and CNES; who have directly and indirectly contributed to the improvement of this manuscript.

References

[1] H. N. Abramson. The Dynamic Behavior of Liquids in Moving Containers. With applications to Space Vehicle Technology. Technical report, 1966.

[2] Helmut F. Bauer. Stability Boundaries Of Liquid-Propelled Space Vehicles With Sloshing. *AIAA Journal*, 1(7):1583–1589, 1963.

[3] Helmut F. Bauer. Fluid oscillations in the containers of a space vehicle and their influence upon stability. Technical report, National Aeronautics and Space Administration, 1964.

[4] John H. Blakelock. *Automatic Control of Aircraft and Missiles*. Wiley, New York, 2nd ed edition, 1991.

[5] Jean-Luc Boiffier. *The Dynamics of Flight: The Equations*. Wiley, Chichester [England]; New York, 1998.

[6] Rudolf Brockhaus. *Flugregelung*. Springer-Verlag, 2013.

[7] Franklin T. Dodge. *The New "Dynamic Behavior of Liquids in Moving Containers"*. Southwest Research Inst. San Antonio, TX, 2000.

[8] Etienne Dumont, Shinji Ishimoto, Michel Illig, Marco Sagliano, Marco Solari, Tobias Ecker, Hauke Martens, Sven Krummen, Jean Desmariaux, Yasuhiro Saito, Moritz Ertl, Josef Klevanski, Bodo Reimann, Svenja Woicke, René Schwarz, David Seelbinder, Markus Markgraf, Johannes Riehmer, Benjamin Braun, and Moritz Aicher. CALLISTO: Towards reusability of a rocket stage: Current status. In *33rd ISTS Conference*, Beppu, Japan, March 2022.

DOI: 10.13009/EUCASS2023-549

[9] Etienne Dumont, Shinji Ishimoto, Pascal Tatiossian, Josef Klevanski, Bodo Reimann, Tobias Ecker, Lars Witte, Johannes Riehmer, Marco Sagliano, Sofia Giagkozoglou, Ivaylo Petkov, Waldemar Rotärmel, René Schwarz, David Seelbinder, Markus Markgraf, Jan Sommer, Dennis Pfau, and Hauke Martens. CALLISTO: A Demonstrator for Reusable Launcher Key Technologies. *Transactions of the Japan Society for Aeronautical and Space Sciences, Aerospace Technology Japan*, 19(1):106–115, January 2021.

[10] Stefano Fari, David Seelbinder, and Stephan Theil. Advanced GNC-oriented modeling and simulation of Vertical Landing vehicles with fuel slosh dynamics. *Acta Astronautica*, April 2023.

[11] A.L. Greensite. *Analysis and Design of Space Vehicle Flight Control Systems. Control Theory: Volume II.* Control Theory. Spartan Books, 1970.

[12] Raouf A. Ibrahim. *Liquid Sloshing Dynamics: Theory and Applications*. Cambridge University Press, 2005.

[13] Steven J. Isakowitz, Joseph P. Hopkins, and Joshua B. Hopkins. *International Reference Guide to Space Launch Systems*. American Institute of Aeronautics and Astronautics, Reston, Va, 4th ed edition, 2004.

[14] Shinji Ishimoto, Pascal Tatiossian, and Etienne Dumont. Overview of the CALLISTO Project. In *32nd ISTS and NSAT*, Fukui, Japan, June 2019.

[15] Jiannwoei Jang. Mechanical Slosh Models for Rocket-Propelled Spacecrafts. In *AIAA Guidance, Navigation, and Control (GNC) Conference*, Guidance, Navigation, and Control and Co-located Conferences. American Institute of Aeronautics and Astronautics, August 2013.

[16] Reza N. Jazar. *Theory of Applied Robotics*. Springer US, Boston, MA, 2010.

[17] R.N. Jazar. *Theory of Applied Robotics: Kinematics, Dynamics, and Control*. Springer International Publishing, 2022.

[18] Sven Krummen, Jean Desmariaux, Yasuhiro Saito, Marcelo Boldt, Lale Evrim Briese, Nathalie Cesco, Christophe Chavagnac, Elisa Cliquet-Moreno, Etienne Dumont, Tobias Ecker, Silas Eichel, Moritz Ertl, Sofia Giagkozoglou, Thilo Glaser, Christian Grimm, Michel Illig, Shinji Ishimoto, Josef Klevanski, Norbert Lidon, Olaf Mierheim, Jean-François Niccolai, Siebo Reershemius, Bodo Reimann, Johannes Riehmer, Marco Sagliano, Henning Scheufler, Anton Schneider, Silvio Schröder, René Schwarz, David Seelbinder, Malte Stief, Jens Windelberg, and Svenja Woicke. Towards a Reusable First Stage Demonstrator: CALLISTO - Technical Progresses & Challenges. In *Proceedings of the International Astronautical Congress, IAC*, Dubai, VAE, October 2021.

[19] Henri Lazennec. *Pilotage Des Missiles et Des Véhicules Spatiaux*. Dunod, 1966.

[20] Allan Lee, Alan Strahan, Rebekah Tanimoto, and Arturo Casillas. Preliminary Characterization of the Altair Lunar Lander Slosh Dynamics and Some Implications for the Thrust Vector Control Design. In *AIAA Guidance, Navigation, and Control Conference*, Guidance, Navigation, and Control and Co-located Conferences. American Institute of Aeronautics and Astronautics, August 2010.

[21] Jose Alfredo Maces Hernandez, Marco Sagliano, Ansgar Heidecker, David Seelbinder, Markus Schlotterer, Stefano Fari, Stephan Theil, Svenja Woicke, and Etienne Dumont. Ascent Flight Control System for Reusable Launch Vehicles: Full Order and Structured H∞ Designs. In *11th International ESA Conference on Guidance, Navigation & Control Systems*, Sopot, Poland, June 2021.

[22] Lukas Opp, Henning Scheufler, Malte Stief, and Jens Gerstmann. Functional and thermal 1D modeling of a reusable LH2-tank using EcosimPro/ESPSS and comparison to CFD results. In *8th Space Propulsion Conference*, Estoril, Portugal, May 2022.

[23] Jing Pei. Analytical Investigation of Propellant Slosh Stability Boundary on a Space Vehicle. *Journal of Spacecraft and Rockets*, 58(5):1514–1521, September 2021.

[24] Mahmut Reyhanoglu. Modelling and control of space vehicles with fuel slosh dynamics. In Jason Hall, editor, *Advances in Spacecraft Technologies*, chapter 24. IntechOpen, Rijeka, 2011.

[25] J. R. Roberts, Eduardo R. Basurto, and P.-Y. Chen. Slosh design handbook, I. Technical report, 1966.

[26] Marco Sagliano, José A. Macés Hernández, Stefano Farì, Ansgar Heidecker, Markus Schlotterer, Svenja Woicke, David Seelbinder, Sven Krummen, and Etienne Dumont. Unified-Loop Structured H-Infinity Control for Aerodynamic Steering of Reusable Rockets. *Journal of Guidance, Control, and Dynamics*, 46(5):815–837, 2023.

DOI: 10.13009/EUCASS2023-549

[27] Marco Sagliano, Taro Tsukamoto, Jose Alfredo Maces Hernandez, David Seelbinder, Shinji Ishimoto, and Etienne Dumont. Guidance and Control Strategy for the CALLISTO Flight Experiment. In *8th EUCASS CONFERENCE FOR AERONAUTICS AND AEROSPACE SCIENCES*, Madrid, Spain, July 2019. EUCASS Association.

[28] Hanspeter Schaub and John L. Junkins. *Analytical Mechanics of Space Systems*. American Institute of Aeronautics and Astronautics, Reston ,VA, January 2009.

[29] Bruno Siciliano and Oussama Khatib, editors. *Springer Handbook of Robotics*. Springer International Publishing, Cham, 2016.

[30] Brian L Stevens, Frank L Lewis, and Eric N Johnson. *Aircraft Control and Simulation: Dynamics, Controls Design, and Autonomous Systems*. John Wiley & Sons, 2015.

[31] Eric Stoneking. Newton-Euler Dynamic Equations of Motion for a Multi-body Spacecraft. In *AIAA GNC Conference*, Hilton Head, SC, August 2007.

[32] Martin J. L. Turner. *Rocket and Spacecraft Propulsion: Principles, Practice and New Developments*. Springer-Praxis Books in Astronautical Engineering. Springer, published in association with Praxis Pub, Berlin ; New York, 3rd ed edition, 2009.

[33] H. Q. Yang and John Peugeot. Propellant Sloshing Parameter Extraction from Computational-Fluid-Dynamics Analysis. *Journal of Spacecraft and Rockets*, 51(3):908–916, May 2014.

[34] Deng-Yun Yu, Ze-Zhou Sun, and He Zhang. *Technology of Lunar Soft Lander*. Springer, 2021.

[35] Honghua Zhang and Zeguo Wang. Attitude control and sloshing suppression for liquid-filled spacecraft in the presence of sinusoidal disturbance. *Journal of Sound and Vibration*, 383:64–75, November 2016.